



Self-duality properties, localization centers, and magnetic energy of the electronic wave functions at small magic angles in twisted bilayer graphene

Leonardo A. Navarro-Labastida and Gerardo G. Naumis ^{*}

*Depto. de Sistemas Complejos, Instituto de Física, Universidad Nacional Autónoma de México (UNAM),
Apdo. Postal 20-364, 01000, CDMX, México*

 (Received 12 September 2023; revised 13 December 2023; accepted 15 December 2023; published 3 January 2024)

Twisted bilayer graphene (TBG) is known for exhibiting highly correlated phases at magic angles due to the emergence of flat bands that enhance electron-electron interactions. The connection between magic angles and the quantum Hall effect remains a topic of ongoing research. In the TBG chiral model, electronic wave function properties depend on a single parameter (α), inversely proportional to the relative twist angle between the two graphene layers (θ), which includes the interlayer interaction strength. In previous studies, as the twist angles approached small values, strong confinement and a convergence to coherent Landau states were observed. However, the origin of these phenomena remained elusive. In this paper, we explore flat band electronic modes, revealing that flat band states exhibit self-duality; they are coherent Landau states in reciprocal space and exhibit minimal dispersion, with standard deviation $\sigma_k = \sqrt{3\alpha/2\pi}$ as $\theta \rightarrow 0$. Subsequently, by symmetrizing the wave functions and considering the squared TBG Hamiltonian, the strong confinement observed in the $\theta \rightarrow 0$ limit is explained. This confinement arises from the combination of the symmetrized squared norm of the moiré potential and the quantized orbital motion of electrons, effectively creating a quantum well. The ground state of this well, located at non-high-symmetry spots, corresponds to a Landau level. Furthermore, we demonstrate that the problem is physically analogous to an electron attached to a non-Abelian SU(2) gauge field with underlying C_3 symmetry. In regions of strong confinement, the system can be considered Abelian, aligning with the picture of a simple harmonic oscillator. This allows us to define a magnetic energy in which the important role of the wave function parity and gap closing at nonmagic angles is revealed. Finally, we investigate the transition from the original non-Abelian nature to an Abelian state by artificially changing the pseudomagnetic vector components from an SU(2) to a U(1) field, which alters the sequence of magic angles. An experimental proposal is made to measure such effects.

DOI: [10.1103/PhysRevB.109.035402](https://doi.org/10.1103/PhysRevB.109.035402)

I. INTRODUCTION

Superconductivity in twisted bilayer graphene (TBG) is known to occur when the rotation angle between layers creates a flat band where electrons exhibit zero group velocity [1]. Such angles are known as magic angles. This significant discovery has underscored the importance of two-dimensional (2D) materials in gaining insight into unconventional superconductivity observed in cuprates and heavy fermion systems. These materials share similar quantum phase diagrams and present a paradigm in the study of moiré materials [1–3]. After the discovery of superconductivity in TBG [1], authors of subsequent studies have confirmed the crucial role of flat bands in the emergence of unconventional superconductivity and strongly correlated phases in twisted multilayer graphene systems [2,4–25]. TBG flat bands, also referred to as zero-mode states, exhibit mathematical similarities with the ground state of the quantum Hall effect (QHE) [26–28]. Magic angles are known to follow a remarkable $\frac{3}{2}$ sequence or quantization rule, characterized by the Fermi velocity vanishing and the emergence of flat bands [26–30].

Tarnopolsky *et al.* [26] established the simplest model for magic angles in TBG by disabling one of the interlayer hoppings. This model played a critical role in elucidating the underlying symmetries, including intralayer inversion symmetry and the parity of magic angles, and enabled a more in-depth analysis of the zero-mode wave function [27,31].

Zero energy modes at magic angles have been investigated in many recent works [4,13,15,17,18,26,27,32–38]. There were mathematical hints for a possible connection with the QHE and the lowest Landau level [26–28,39,40]. Authors of other works revealed interesting connections with fractional QHE (FQHE), topological matter, Weyl semimetals, Floquet systems, anomalous edge states, strain effects, and electrically tunable gauge fields [5,7,38,41–53].

Researchers in magic-angle TBG have indeed established a close relationship between the squared Hamiltonian of this system and the quantum harmonic oscillator and the QHE [28]. The ground state corresponds to a flat band in which the wave function converges into coherent Landau-level states of the QHE. Another significant outcome was the explanation of the $\frac{3}{2}$ magic angle recurrence rule through the use of scaling arguments, revealing its intimate connection to the quantization of angular momentum [28]. Consequently, for each magic angle, there exists an almost well-defined attached angular

^{*}naumis@fisica.unam.mx

quantum number which can be interpreted as interlayer currents [28,30]. This explanation of the fundamental principles behind the magic-angle phenomenon offers valuable insight into addressing fundamental questions at the intersection of the FQHE and unconventional superconductivity, which are currently the focus of intense study in strongly correlated systems [54].

However, despite our previous works [28,30,55], several questions remain unanswered. One of these questions pertains to the mechanism behind the strong localization of wave functions in magic-angle invariant spots once the lattice is properly scaled by the parameter α , which encapsulates the energetic interaction coupling between layers and the angle. Additionally, we have yet to explore the consequences of nearly coherent Landau states. Here, we show that zero modes behave as minimal dispersion packets as expected. We also explain how the wave function confinement arises around certain localization centers due to an effective potential produced by the moiré potential and the orbital motion of the electron. Moreover, we show that the magic-angle order parity is a crucial property associated with flat bands in TBG. We also establish some connections between the angular momentum and non-Abelian pseudomagnetic fields.

This paper is divided as follows. Section II introduces the Hamiltonian for the chiral TBG (cTBG) model and the pseudomagnetic field that emerges due to the effect of the parameter α . Section III finds self-duality localization properties between reciprocal and real space and demonstrates that zero-mode states are coherent Landau states. Section IV analyzes confinement conditions for the electronic wave function in the asymptotic limit $\alpha \rightarrow \infty$ and the symmetries of the zero energy wave function. Section V explores the non-Abelian nature of TBG and its connection with the magnetic QHE. Section VI analyzes the non-Abelian nature of the pseudomagnetic field by changing artificially its structure to make it more Abelian and how the scaling and recurrence are modified. Finally, Sec. VII gives some conclusions and further research directions.

II. CHIRAL SQUARED TBG HAMILTONIAN

The Bistritzer-MacDonald (BM) Hamiltonian provided a low-energy model for TBG and unveiled the existence of magic angles [29]. To account for structural relaxation effects, the tunneling between layers in the AA stacking regions can be set to zero, resulting in a model that exhibits an additional chiral symmetry. This reduced model is referred to as the cTBG or Tarnopolsky-Kruchkov-Vishwanath (TKV) model [26]. In the chiral basis, the bispinor is $\Phi(\mathbf{r}) = [\psi_1(\mathbf{r}), \psi_2(\mathbf{r}), \chi_1(\mathbf{r}), \chi_2(\mathbf{r})]^T$, where indexes 1, 2 denote each graphene layer, and $\psi_j(\mathbf{r})$ and $\chi_j(\mathbf{r})$ are the Wannier orbitals on each sublattice of the unit cell of graphene.

The chiral Hamiltonian is given by [26,32,56],

$$\mathcal{H} = \begin{bmatrix} 0 & D^*(-\mathbf{r}) \\ D(\mathbf{r}) & 0 \end{bmatrix}, \quad (1)$$

where the zero-mode operator is defined as

$$D(\mathbf{r}) = \begin{bmatrix} -i\bar{\partial} & \alpha U(\mathbf{r}) \\ \alpha U(-\mathbf{r}) & -i\bar{\partial} \end{bmatrix}, \quad (2)$$

with $\bar{\partial} = \partial_x + i\partial_y$. The coupling potential between layers is

$$U(\mathbf{r}) = \sum_{v=1}^3 \exp[i\phi(v-1)] \exp(-i\mathbf{q}_v \cdot \mathbf{r}), \quad (3)$$

where the phase factor is $\phi = 2\pi/3$, and the vectors are given by

$$\begin{aligned} \mathbf{q}_1 &= k_\theta(0, -1), \\ \mathbf{q}_2 &= k_\theta \left(\frac{\sqrt{3}}{2}, \frac{1}{2} \right), \\ \mathbf{q}_3 &= k_\theta \left(-\frac{\sqrt{3}}{2}, \frac{1}{2} \right), \end{aligned} \quad (4)$$

where the moiré modulation vector is $k_\theta = 2k_D \sin \frac{\theta}{2}$, with $k_D = \frac{4\pi}{3a_0}$ the magnitude of the Dirac wave vector, and a_0 is the lattice constant of monolayer graphene. The cTBG model has only α as a parameter, defined as $\alpha = \frac{w_1}{v_0 k_\theta}$, where $w_1 = 110$ meV is the interlayer coupling of stacking AB/BA, and $v_0 = \frac{19.81 \text{ eV}}{2k_D}$ is the Fermi velocity. The diagonal operators ∂ and $\bar{\partial}$ are dimensionless, as Eq. (1) is written using units where $v_0 = 1$, $k_\theta = 1$. The twist angle only enters in the dimensionless parameter α and scaling energy ϵ/α . In k space, the moiré Brillouin zone (mBZ) reciprocal vectors are

$$\begin{aligned} \mathbf{b}_{1,2} &= \mathbf{q}_{2,3} - \mathbf{q}_1 = \left(\pm \frac{\sqrt{3}}{2}, \frac{3}{2} \right), \\ \mathbf{b}_3 &= \mathbf{q}_3 - \mathbf{q}_2 = (\sqrt{3}, 0), \end{aligned} \quad (5)$$

as the moiré reciprocal vectors. Some important high-symmetry points of the mBZ are $\mathbf{K} = (0, 0)$, $\mathbf{K}' = -\mathbf{q}_1$, and $\Gamma = \mathbf{q}_1$ [30]. It is also convenient to define a set of unit vectors \mathbf{q}_v^\perp perpendicular to the set \mathbf{q}_v and defined as

$$\begin{aligned} \mathbf{q}_1^\perp &= (1, 0), \\ \mathbf{q}_2^\perp &= \left(-\frac{1}{2}, \frac{\sqrt{3}}{2} \right), \\ \mathbf{q}_3^\perp &= \left(-\frac{1}{2}, -\frac{\sqrt{3}}{2} \right). \end{aligned} \quad (6)$$

The moiré vector unit cells are given by $\mathbf{a}_{1,2} = (4\pi/3k_\theta)(\frac{\sqrt{3}}{2}, \frac{1}{2})$. Note that $\mathbf{q}_v \cdot \mathbf{a}_{1,2} = -\phi$ for $v = 1, 2, 3$. In our previous works [28,30,55], we demonstrated that squaring the Hamiltonian \mathcal{H} allows us to simplify it into a 2×2 matrix that we call the squared Hamiltonian H^2 . In this paper, we introduce notation changes in the definitions used inside H^2 . The reasons will become evident later on. Here, H^2 is given by

$$H^2 = \begin{bmatrix} -\nabla^2 + \alpha^2(\mathbf{A}^2 + i[A_x, A_y]) & \alpha(-2i\mathbf{A}_- \cdot \nabla + \nabla \times \mathbf{A}_-) \\ \alpha(-2i\mathbf{A}_+ \cdot \nabla + \nabla \times \mathbf{A}_+) & -\nabla^2 + \alpha^2(\mathbf{A}^2 - i[A_x, A_y]) \end{bmatrix}, \quad (7)$$

where we defined

$$\mathbf{A}_{\pm} \equiv \mathbf{A}(\pm\mathbf{r}) = \sum_{\nu=1}^3 \exp(\pm i\mathbf{q}_{\nu} \cdot \mathbf{r}) \mathbf{q}_{\nu}^{\perp}. \quad (8)$$

Here, \mathbf{A}_{\pm} is a pseudomagnetic vector potential with C_3 symmetry, and $\mathbf{A}^2 = |\mathbf{A}_{\pm}|^2$. The squared norm of the coupling potential is an effective intralayer confinement potential:

$$|U(\pm\mathbf{r})|^2 = \mathbf{A}^2 \mp i[A_x, A_y], \quad (9)$$

where the confinement potential $|U(\pm\mathbf{r})|^2$ is separated into its purely symmetric $\mathbf{A}^2(\mathbf{r})$ and antisymmetric $i[A_x, A_y]$ parts defined as

$$\begin{aligned} \mathbf{A}^2(\mathbf{r}) &= 3 - \sum_{\nu} \cos(\mathbf{b}_{\nu} \cdot \mathbf{r}), \\ \Delta(\mathbf{r}) &= \sqrt{3} \sum_{\nu} (-1)^{\nu} \sin(\mathbf{b}_{\nu} \cdot \mathbf{r}). \end{aligned} \quad (10)$$

Here, $\Delta(\mathbf{r}) = i[A_x, A_y]$, where A_x and A_y are the non-Abelian components of the $SU(2)$ pseudomagnetic vector potential (see Appendix A). It is important to remark that the pseudomagnetic vector potential satisfies the relation $\nabla \cdot \mathbf{A}_{\pm} = 0$ and thus is a Coulomb gauge-invariant field, and $\nabla \times \mathbf{A}_{+} = \mathbf{B}_{+}$ (layer 1) and $\nabla \times \mathbf{A}_{-} = \mathbf{B}_{-}$ (layer 2). The magnetic field is thus given by

$$\mathbf{B}_{\pm} = \mathbf{B}(\pm\mathbf{r}) = \pm i \sum_{\nu} \exp(\pm i\mathbf{q}_{\nu} \cdot \mathbf{r}) \mathbf{e}_z, \quad (11)$$

where we have used the identity $\mathbf{e}_z = \mathbf{q}_{\nu} \times \mathbf{q}_{\nu}^{\perp}$, and \mathbf{e}_z is a unit vector in the direction perpendicular to the graphene plane.

Notice that squaring the chiral TBG model is akin to a supersymmetric transformation [57–61], which seems to play a role in the proposed equivalence between the squared TBG electron Hamiltonian and an electron coupling to a $SU(2)$ non-Abelian pseudomagnetic field [55].

III. SELF-DUALITY PROPERTIES AND CONVERGENCE INTO COHERENT LANDAU STATES

It has been demonstrated that TBG has Landau levels [15,25,37,62] that play a role in its remarkable properties [16,18,23,38,48,49,54,63]. However, there are some gaps related to the understanding of electronic localization in TBG from the perspective of one particle.

For example, in a recent previous paper, we demonstrated that the wave function in TBG exhibits an almost coherent Landau state nature with a dispersion $\sigma = 1/\sqrt{3\alpha}$, which is only reached in the asymptotic limit [28]. Here, we discuss some properties of the wave functions in this limit and their relationship with coherent states.

Coherent states are self-dual in the sense that their Fourier transforms in reciprocal space look similar to in real space but with inverted parameters. As a consequence, they satisfy the minimal uncertainty relation between real and momentum space. Let us now explore such a property for TBG zero modes.

In Fig. 1, we present the evolution of the electronic density in real space $[\rho(\mathbf{r})]$ for different magic angles in the line $\mathbf{r} = (0, y)$. We observe that $\rho(\mathbf{r})$ seems to be mostly made from Gaussian functions centered at different locations. To

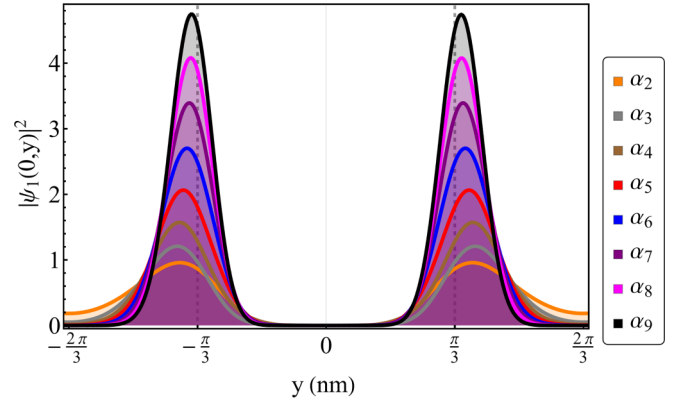


FIG. 1. Electronic density $\rho(\mathbf{r})$ along the y axis for layer 1. The solid curves with shaded areas are the normalized numerical solutions of the zero mode equation for the indicated magic angles. The thick vertical lines (black lines) indicate the limiting localization points $\mathbf{R} \approx \pm\pi/3$. As the magic angle order increases, the density becomes sharply peaked.

further elaborate on this, in Fig. 2, we present the logarithm of the electronic probability density in real space for the ninth magic angle α_9 around one of the localizations centers. Here, we used normalized coordinates as $\frac{y-\mathbf{R}}{\sqrt{\alpha}}$, where $\mathbf{R} \approx 1.047$ is the position of one of the numerically found maximums (this value suggests that $\mathbf{R} \approx \pi/3$, but we do not have a proof of this conjecture). For comparison, in Fig. 2, we plot the logarithm of a normalized Gaussian with the same dispersion.

In Fig. 3, we plot the logarithm of $\rho(\mathbf{r})$ from the second to ninth magic angles written in normalized coordinates, i.e., with zero mean and standard deviation one. It is important to note that, in Fig. 3, we are using a logarithm scale. From Figs. 1–3, we conclude that the density is almost made from Gaussians as also follows from an analysis of the zero-mode equations [28].

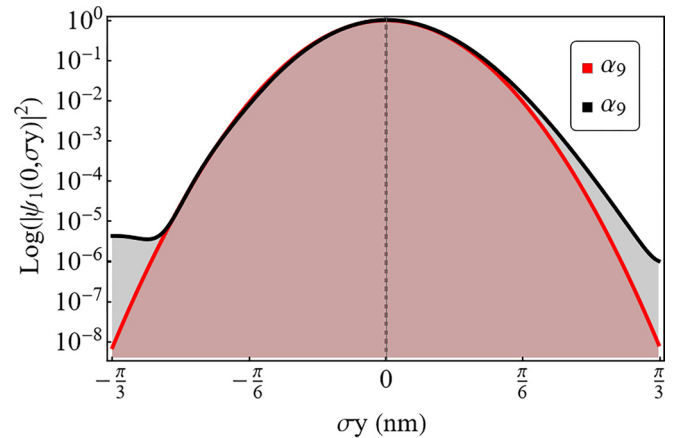


FIG. 2. Electronic density, in log scale, for the ninth-order magic angle α_9 at the Γ point and along the y axis. The black line is the numerical data obtained from the Hamiltonian. A normalized y' variable was used such that $\sigma y = (y' - 1.047)/\sqrt{3\alpha}$. The red curve is a Gaussian with center at $y = 0$ and unitary standard deviation in scaled coordinates.

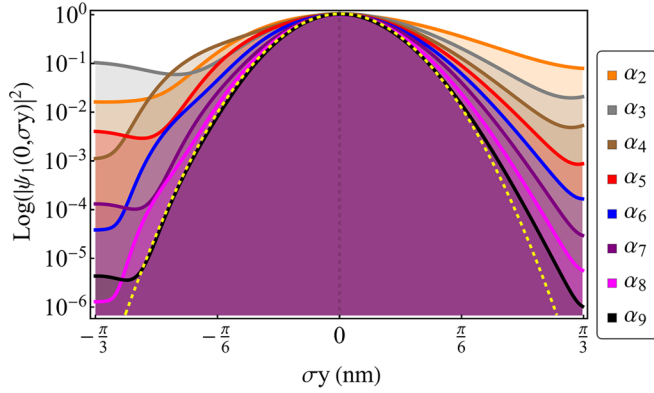


FIG. 3. Electronic density, in log scale, from the second to ninth magic angles for the Γ point and as a function of the position along the y axis rescaled by the standard deviation σ . For simplicity, the normalized variable was used such that $\sigma y = (y' - 1.047)/\sqrt{3\alpha}$ to center the Gaussian around the origin. Notice the convergence into a Gaussian. The dashed curve is a Gaussian with center at $y = 0$ and unitary standard deviation in scaled coordinates.

Figure 2 also reveals that $\rho(\mathbf{r})$ exhibits a fat-tail decay. Interestingly, this characteristic makes the electronic density somewhat akin to the velocity distribution fluctuations in turbulence [64]. As shown in Fig. 3, the tails at $\sigma y = \pm\pi/3$ decrease with the magic-angle order. For example, at the magic angle α_8 , the tail at $\sigma y = \pi/3$ is nearly six orders of magnitude smaller than the maximum, making its deviation from a Gaussian distribution imperceptible upon simple inspection in a linear scale plot, as seen in Fig. 1. A further confirmation of this can be obtained by looking at the kurtosis of $\rho(\mathbf{r})$, defined as $\text{Kurtosis} = \mu_4/\sigma^4$, where μ_4 is the fourth moment of the density. For a Gaussian, the kurtosis is exactly 3. Figure 4 presents the evolution of the function $|\text{Kurtosis} - 3|$ as a function of α , showing that, indeed, convergence to a Gaussian is obtained.

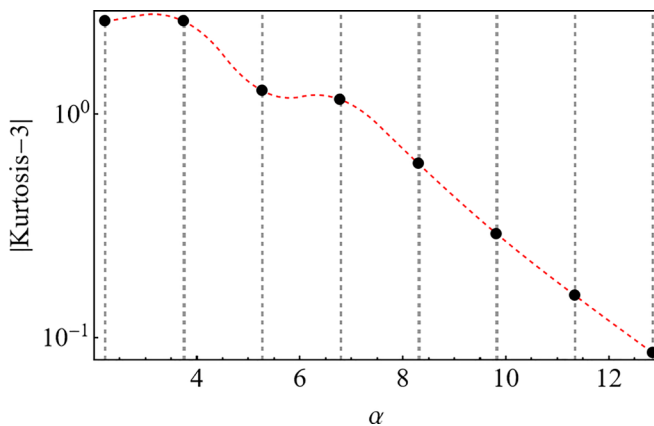


FIG. 4. Kurtosis obtained from the real-space electronic density from the second to ninth magic angles for the Γ point as a function of α . Black vertical lines indicate magic angles. For higher magic angles, $|\text{Kurtosis} - 3| \rightarrow 0$, corroborating that $\rho(\mathbf{r})$ converges into a normal distribution. Black points are numerical results, and the red curve is an interpolation to the numerical data.

As the positions of maximal electronic density probability near the origin are located at $\mathbf{R} \approx \pm 1.047\mathbf{q}_v$, the density can be approximated by a Gaussian distribution near \mathbf{R} as

$$|\psi(\mathbf{r})|^2 \approx \frac{3A_M}{2\pi\sigma} \exp\left(-\frac{1}{2\sigma^2}|\mathbf{r} \pm \mathbf{R}|^2\right), \quad (12)$$

where $A_M = 8\pi^2/(3\sqrt{3})$ is the normalized moiré unit cell area, and $\sigma = 1/\sqrt{3\alpha}$ is the standard deviation. Note that Eq. (12) is independent of α . The fat tails are in fact explained by the known analytical form of zero-mode wave functions. According to Refs. [27,33,62], zero-mode wave functions can always be written as

$$|\psi(\mathbf{r})|^2 = \frac{A_M}{2\pi\sigma} \exp\left(-\frac{1}{2\sigma^2}|\mathbf{r} \pm \mathbf{R}|^2\right) |W_\alpha(\mathbf{r})|^2, \quad (13)$$

where $W_\alpha(\mathbf{r})$ is an α -dependent function written in terms of the Weierstrass σ function and on the zero mode at the \mathbf{K} point [27], $\psi_{\mathbf{K}}(\mathbf{r})$. This last wave function is, unfortunately, not analytically known. However, these analytical findings are consistent with our numerical results only if the fat tails are generated by the function $W_\alpha(\mathbf{r})$. Equation (13) is interesting because it enables the production of wave function overlaps, while at the same time, the electron density is strongly concentrated in specific regions. In that sense, these states share similarities with other flat-band states, like compact localized states [65], confined states [66,67], and time-dependent flat Floquet bands [68,69].

Notice that the tails in Figs. 2 and 3 exhibit asymmetry, and there are several reasons for this. By examining Fig. 1, it is evident that the two Gaussians centered at $\pm\mathbf{R}$ overlap more significantly near the origin than with other Gaussians centered in neighboring unitary cells. Consequently, the asymmetry serves as an indirect signature of varying distances to other localization centers. Furthermore, there is a contribution from the asymmetry of the potential $U(\mathbf{r})$, as AB regions differ from BA regions. In fact, magic angles are obtained whenever the wave function has zeros in the AB stacking point in both layers, while in general, it is not zero in the BA stacking point [26]. Additionally, observe in Fig. 3 how the parity of the magic-angle order influences the fat tail at $\sigma y \rightarrow -\pi/3$. This effect is a consequence of the magnetic energy term discussed in Sec. V.

Now we explore the self-dual properties of zero modes by looking at the reciprocal space. As the wave functions follow Bloch's theorem, they can be written as [26]

$$\begin{aligned} \Psi_{\mathbf{k}}(\mathbf{r}) &= \begin{bmatrix} \psi_{\mathbf{k},1}(\mathbf{r}) \\ \psi_{\mathbf{k},2}(\mathbf{r}) \end{bmatrix} \\ &= \sum_{l,n} \begin{bmatrix} a_{ln} \\ b_{ln} \exp(i\mathbf{q}_1 \cdot \mathbf{r}) \end{bmatrix} \exp[i(\mathbf{K}_{ln} + \mathbf{k}) \cdot \mathbf{r}], \end{aligned} \quad (14)$$

where a_{ln} and b_{ln} are Fourier coefficients for layers 1 and 2, respectively, \mathbf{k} is a generic reciprocal wave vector, and $\mathbf{K}_{ln} = l\mathbf{b}_1 + n\mathbf{b}_2$. The vectors \mathbf{b}_1 and \mathbf{b}_2 are the two mBZ vectors defined in Sec. II.

In Fig. 5(a), we present the Fourier coefficient squared norm for the zero-mode wave function at the Γ point for

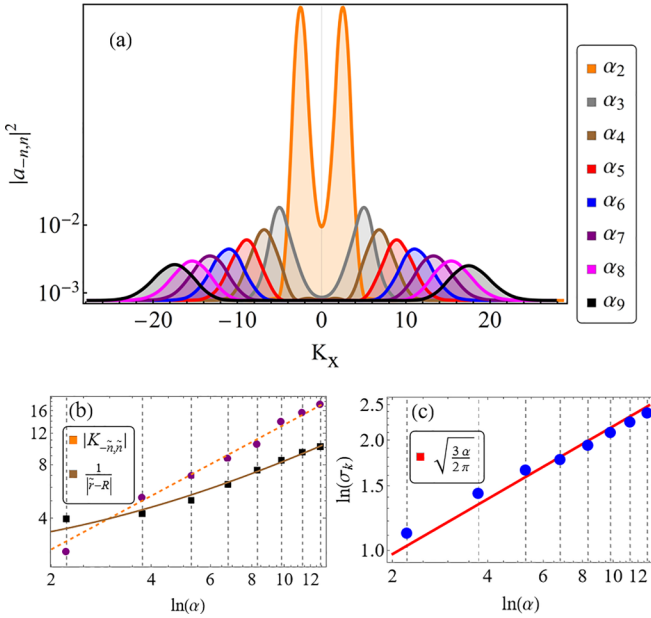


FIG. 5. Fourier coefficients in reciprocal space in the direction $\mathbf{K}_{-\tilde{n},\tilde{n}} = \tilde{n}\mathbf{b}_3$. (a) shows the squared norm of Fourier coefficients $|a_{-n,n}|^2$ from the second to ninth magic angles along the direction $\mathbf{K}_x = n(\mathbf{b}_2 - \mathbf{b}_1)$. (b) presents the convergence, in log-log scale, for the values $|K_{-\tilde{n},\tilde{n}}|$ (purple dots) and $1/|\tilde{\mathbf{r}} - \mathbf{R}|$ (black squares) with $\mathbf{R} \approx 1.047\mathbf{q}_1$. The associated lines for each marker are the linear fits $|K_{-\tilde{n},\tilde{n}}| \approx 1.34\alpha$ (orange dashed) and $1/|\tilde{\mathbf{r}} - \mathbf{R}| \approx 2.1 + 0.6\alpha$ (brown solid). (c) shows the standard deviation in the log-log scale for the Gaussian distribution at the maximum point $\mathbf{K}_{-\tilde{n},\tilde{n}}$. Here, it is numerically proved that $\sigma_k = \sqrt{\frac{3\alpha}{2\pi}}$ in k space with the relation $\sigma_k = 1/(\sqrt{2\pi}\sigma_r)$, where the indexes k and r represent k or real space, respectively. This result shows that solutions are coherent states because they minimize the dispersion $\sigma_r\sigma_k = 1/\sqrt{2\pi}$ thus, with minimal uncertainty relation $\sigma_r^2\sigma_k^2 = \hbar$, where $\hbar = h/2\pi$ using natural units $h = 1$ as the Planck's constant. Both (b) and (c) are representatives of the numerical data accuracy. For (b), the fit for $\mathbf{K}_{-\tilde{n},\tilde{n}}$ has an error of $\sim 3\%$, while for $1/|\tilde{\mathbf{r}} - \mathbf{R}|$, it is $\sim 5\%$. In (c), the numerical data fit deviates $\sim 5\%$ from the approximate limiting theoretical result (red line) $\sigma_k = \sqrt{\frac{3\alpha}{2\pi}}$.

$\mathbf{K}_x = n(\mathbf{b}_2 - \mathbf{b}_1)$, given by $|a_{-n,n}|^2$, for magic angles between α_2 and α_9 . We can clearly see the Gaussian shape of the peaks, which turn out to be similar to the wave function in real space seen in fig. 2 of our previous work [28]. This is in agreement with the idea of states converging into coherent states. As we can see, the coefficients $|a_{-n,n}|^2$ for α_2 are strongly localized, while for higher magic angles α_9 , the symmetric Gaussians of the two original mirrors are quite separated, while the dispersion increases. For the real-space case, the situation is reversed because the Gaussians are more localized, and their dispersion is reduced for higher magic angles (see Ref. [28]). In Fig. 5(b), we show the peak position of the Gaussian in k space ($|\mathbf{K}_{-\tilde{n},\tilde{n}}|$), where $(-\tilde{n}, \tilde{n})$ correspond to the reciprocal point with maximal norm Fourier coefficient, i.e., the positions of the maxima in reciprocal space along one direction. This is compared with the inverse of the difference between the wave function peak positions in real space ($\tilde{\mathbf{r}}$) and the limiting localization center for $\alpha \rightarrow \infty$, i.e., we plot $1/|\tilde{\mathbf{r}} - \mathbf{R}|$.

On the other hand, Fig. 5(c) presents the dispersion in k space, denoted by σ_k , as a function of α , showing that the dispersion increases with α . This result can be explained as follows. In fig. 3 of our previous work [28], numerical data were presented for the dispersion in real space. It was shown that the dispersion in real space converges to $\sigma = 1/\sqrt{3\alpha}$. Such a result was also obtained analytically by studying the potential near the origin [28]. Very good agreement was found between the theoretical prediction $\sigma = 1/\sqrt{3\alpha}$ and the numerical data.

Now we use that the Fourier transform of a Gaussian is another Gaussian with inverse standard deviation to obtain that the dispersion in reciprocal space goes as

$$\sigma_k = \sqrt{\frac{3\alpha}{2\pi}}, \quad (15)$$

in agreement with Fig. 5(c). In both Figs. 5(b) and 5(c), the vertical lines indicate magic angles. The solid lines are the theoretical results, and the markers are the numerical results. We use the log-log scale for visual convenience. From these results, we can conclude that, indeed, our states converge into coherent states because they satisfy Heisenberg's uncertainty relation with minimal dispersion, i.e.,

$$\sigma_r\sigma_k \approx \sqrt{\frac{1}{3\alpha}} \sqrt{\frac{3\alpha}{2\pi}} = \sqrt{\frac{1}{2\pi}}, \quad (16)$$

or using natural units $\hbar = 1$ (Planck's constant), we end with

$$\Delta_r\Delta_k \approx \hbar, \quad (17)$$

where $\Delta_r = \sigma_r^2$ and $\Delta_k = \sigma_k^2$. The result \hbar is a consequence of the model because we are treated with a 2D model, and each degree of freedom contributes $\hbar/2$ to the dispersion, in analogy to a 2D quantum harmonic oscillator.

To give more insight into the localization centers in reciprocal space, Fig. 6 presents a color map for the Fourier coefficients $|a_{mn}|^2$ (layer 1) for the Γ -point wave function. From Figs. 6(a) to 6(d) the magic-angle order increases, and the maxima of the Fourier coefficients depart radially from the center. Pink arrows indicate where the sixth localization center lies.

According to these numerical results, the maxima of the electronic probability in k space are near

$$\tilde{n}\mathbf{b}_v \pm 1.047\mathbf{q}_v, \quad (18)$$

and their corresponding rotated versions by $2\pi/3$. In real space, the maxima are at

$$\mathbf{R} \approx \frac{1}{\tilde{n}} \hat{\mathbf{R}}_{-\phi}(\mathbf{b}_v) + 1.047 \hat{\mathbf{R}}_{-\phi}(\mathbf{q}_v). \quad (19)$$

Here, $\hat{\mathbf{R}}_{-\phi}$ represents rotation by an angle $\phi = \frac{2\pi}{3}$ and $\tilde{n} \approx \sqrt{3}\alpha_m/2$. For the other layer, the same behavior occurs with the Fourier coefficients ($|b_{mn}|^2$). Therefore, we can summarize such behavior as follows. As $\alpha \rightarrow \infty$, wave functions become strongly confined in certain spots. In reciprocal space, the confinement is also present but decreases with growing α , and at the same time, the locations of the maxima go to infinity.

From another perspective, the situation here is not different from any other second-order differential equation with periodic potentials. To understand this, first, we observe that,

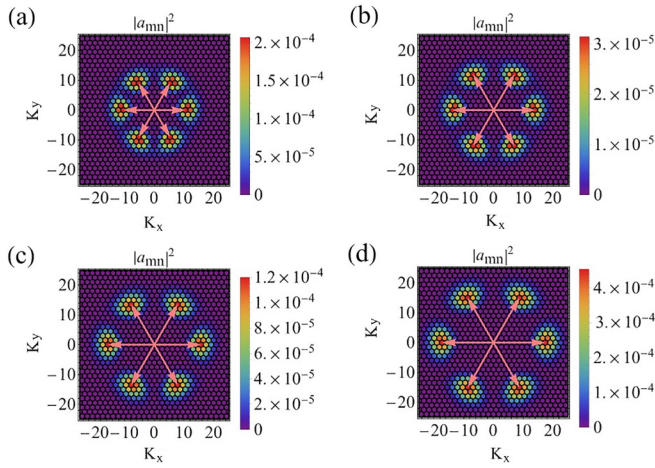


FIG. 6. Fourier coefficient squared norm color map for the zero-mode wave function for high magic angles. (a) $\alpha_6 = 8.313$, (b) $\alpha_7 = 9.829$, (c) $\alpha_8 = 11.345$, and (d) $\alpha_9 = 12.855$. All correspond to the Γ -point coefficients. The arrows indicate the positions of the maximal norm Fourier coefficients and are the centers of the coherent Landau states in reciprocal space. The centers are located at $\tilde{n}\mathbf{b}_\nu \pm 1.047\mathbf{q}_\nu$, where $\tilde{n} \approx \sqrt{3}\alpha_m/2$ for $m \rightarrow \infty$ higher magic angles, and C_3 rotations produce the extra points seen in the figure. Observe how, as the magic angle order grows, the maxima are pushed away from the center.

only for a small coupling parameter α , the maxima of the solution in reciprocal space are found at the reciprocal vectors corresponding to the Fourier components of the underlying potential. In fact, it can be analytically demonstrated that the wave function for the first magic angle is essentially a scaled version of the potential [26,30]. For higher values of the coupling α , the maxima shift to higher harmonics, even if the potential itself does not contain these Fourier components. The argument for this behavior is as follows. In the H^2 eigenvalue equation for $E = 0$, the kinetic energy term given by the Laplacian must have maxima at some \mathbf{K}_{ln} reciprocal vectors that scale as $|\mathbf{K}_{ln}|^2 \sim \alpha^2$ to nullify the potential term $\alpha^2 \mathbf{A}^2(\mathbf{r}) = \alpha^2 [3 - \sum_\nu \cos(\mathbf{b}_\nu \cdot \mathbf{r})]$. Later on, we will show that the commutator term $\alpha^2 \Delta^2(\mathbf{r})$ is not important, while the off-diagonal term, due to the energy equipartition at magic angles, gives a similar contribution [28]. Therefore, the kinetic energy selects which harmonics \mathbf{K}_{ln} are active for a given α . This simple explanation accounts for Eq. (18), as $|\mathbf{K}_{ln}| = |\mathbf{b}_1 + n\mathbf{b}_2| \sim \alpha$ with l and n integers, and for example, in the line $l = -n$, we obtain $n\mathbf{b}_3 \sim \alpha$. As depicted in Fig. 6, magic angles precisely correspond to a new hexagon of harmonics contained in a circle with radius α that becomes active as $\alpha \rightarrow \infty$. A simple and apt analogy for this phenomenon can be drawn from a standard Mathieu ordinary differential equation, which describes a parametric pendulum [70,71]:

$$\frac{d^2}{dt^2} \psi(t) + [a - 2q \cos(2t)] \psi(t) = 0, \quad (20)$$

where $\psi(t)$ is the pendulum displacement at time t , and here, we take $a = 3\alpha^2$ and $q = \alpha^2/2$ to emulate in a bare form the potential $\alpha^2 \mathbf{A}^2(\mathbf{r})$. In this case, the driving term $2q \cos(2t)$ only contains a fundamental frequency $G = 2$ and its negative $G = -2$. No harmonics are present. However, the coupling

parameter α is not only a measure of the parametric driving amplitude but also gives the unperturbed pendulum frequency, i.e., of a harmonic oscillator with frequency $\sqrt{3}\alpha$. As the periodic driving strength increases with α , the harmonic oscillator frequency also increases and now can only become resonant with higher-order harmonics of the driving frequency, even if the potential lacks these Fourier components. The well-known Mathieu equation stability chart in terms of the parameters (a, q) contains such information [70–74]. It features the famous Arnold tongues corresponding to resonances between the driven and undriven oscillator frequencies and their harmonics [71]. These resonances are the equivalent to magic angles.

To delve deeper into such properties, in the following section, we discuss how and why confinement at certain locations in real space arises. As we will see, this question is much more difficult to answer than the locations of the maxima in reciprocal space.

IV. CONFINEMENT AND WAVE FUNCTION SYMMETRIES

As was discussed in the previous section and in previous works [28,30], the wave functions in real space converge into very sharp Gaussian packets which are located at the invariant points \mathbf{R} . In this section, we discuss the origin of this effect as well as some symmetry properties of the wave function required to understand how the confinement arises. Let us show first how, at higher magic angles, the wave function in real space can be decoupled into symmetric and antisymmetric parts. These are spatially located at different regions and depend on the magic-angle order parity. To clarify these points, it is convenient to write the zero-mode equation of the squared Hamiltonian:

$$[-\nabla^2 + \alpha^2(\mathbf{A}^2 + i[A_x, A_y])] \psi_1(\mathbf{r}) + \alpha(-2i\mathbf{A}_- \cdot \nabla + \nabla \times \mathbf{A}_-) \psi_2(\mathbf{r}) = 0. \quad (21)$$

It is noteworthy that the eigenfunctions of \mathcal{H} simultaneously serve as eigenfunctions of H^2 ; however, the reverse is not true. Here, we will work with H^2 because it has more physical relevance for the present discussion; however, the numerical calculations of the wave function that we will present in what follows are in the 4×4 chiral basis of \mathcal{H} . As explained elsewhere [30], any linear combination of degenerate eigenfunctions of \mathcal{H} are solutions of H^2 , so there is a phase involved. Despite this, the electronic density and energy contributions are not affected if they are calculated in H^2 or \mathcal{H} as the phase factor is eliminated.

For simplicity, in this analysis, we will first consider the Γ point. In this case, the symmetry allows us to write $\psi_2(\mathbf{r}) = i\mu_\alpha \psi_1(-\mathbf{r})$, with $\mu_\alpha = \pm 1$ as the magic-angle order parity [26]. For odd-parity magic-angle order, i.e., for α_{2m+1} , we have $\mu_\alpha = +1$, while for even parity, we have $(\alpha_{2m}) \mu_\alpha = -1$.

We now define symmetric or antisymmetric wave functions as $\psi_\pm(\mathbf{r}) = \psi_1(\mathbf{r}) \pm \psi_1(-\mathbf{r})$, and symmetry/antisymmetry non-Abelian pseudomagnetic fields as

$$\mathcal{A}_\pm = \frac{\mathbf{A}_+ \pm \mathbf{A}_-}{2}. \quad (22)$$

Using the previous definitions and the commutator Δ given in Eq. (10), it can be shown that the pair of zero-mode

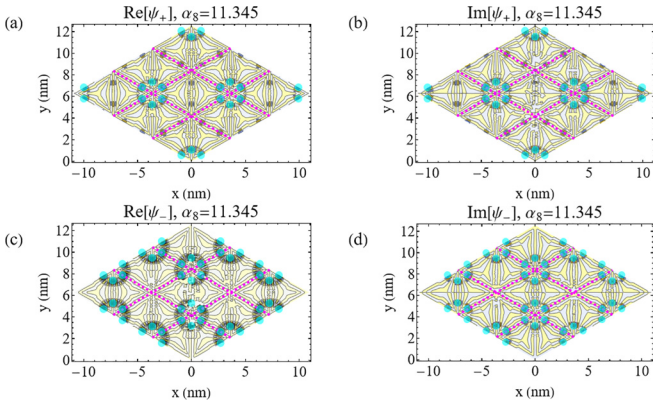


FIG. 7. Symmetric $[\psi_+(\mathbf{r})]$ and antisymmetric $[\psi_-(\mathbf{r})]$ wave functions in a 3×3 unit cell for $\alpha_8 = 11.345$. The blue circles indicate where the electronic wave function is localized, and the dashed lines show unit cells defined by the vectors \mathbf{a}_1 and \mathbf{a}_2 . Symmetric/antisymmetric wave functions are defined as $\psi_{\pm} = \psi_1(\mathbf{r}) \mp i\mu_{\alpha}\psi_2(\mathbf{r})$. Considering the Γ point $\psi_2(\mathbf{r}) = i\mu_{\alpha}\psi_1(-\mathbf{r})$, symmetric/antisymmetric solutions change as $\psi_{\pm} = \psi_1(\mathbf{r}) \pm \psi_1(-\mathbf{r})$. (a) and (b) Real and imaginary parts of the symmetric wave function ψ_+ . (c) and (d) Real and imaginary parts of the antisymmetric wave function ψ_- . Note that symmetric and antisymmetric solutions are almost spatially decoupled.

equations in Eq. (21) can be rewritten as

$$[-\nabla^2 + \alpha^2 \mathbf{A}^2 - i\mu_{\alpha}\alpha(-2i\mathcal{A}_{\mp} \cdot \nabla + \nabla \times \mathcal{A}_{\mp})]\psi_{\pm} + [\alpha^2 \Delta - i\mu_{\alpha}\alpha(-2i\mathcal{A}_{\pm} \cdot \nabla + \nabla \times \mathcal{A}_{\pm})]\psi_{\mp} = 0. \quad (23)$$

Our numerical results in Figs. 7 and 8 highlight that, indeed, the solutions are decoupled spatially in this symmetric or antisymmetric basis. For example, in Fig. 7, the magic

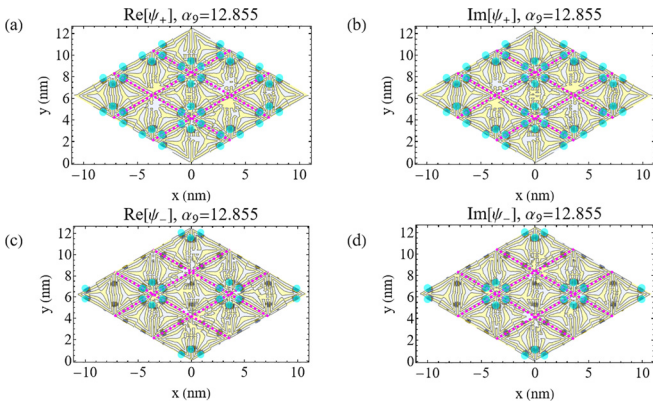


FIG. 8. Symmetric and antisymmetric wave functions in a 3×3 unit cell for $\alpha_9 = 12.855$. The blue circles indicate where the electronic wave function is localized, and the dashed lines show unit cells defined by the vectors \mathbf{a}_1 and \mathbf{a}_2 . Symmetric/antisymmetric wave functions are defined as $\psi_{\pm} = \psi_1(\mathbf{r}) \mp i\mu_{\alpha}\psi_2(\mathbf{r})$. Considering the Γ point $\psi_2(\mathbf{r}) = i\mu_{\alpha}\psi_1(-\mathbf{r})$, symmetric/antisymmetric solutions change as $\psi_{\pm} = \psi_1(\mathbf{r}) \pm \psi_1(-\mathbf{r})$. (a) and (b) Real and imaginary parts of the symmetric wave function ψ_+ . (c) and (d) Real and imaginary parts of the antisymmetric wave function ψ_- . Note that symmetric and antisymmetric solutions are almost decoupled.

angle ($\alpha_8 = 11.345$) has even order parity ($m = 8$), with $\mu_{\alpha} = -1$. In Figs. 7(a) and 7(b), we present the real and imaginary parts, respectively, of the symmetric solution ψ_+ . The blue dots indicate the corresponding maxima. In Figs. 7(c) and 7(d), we present a similar plot for ψ_- . The maxima of ψ_- are in different locations than those in ψ_+ . Moreover, for even parity, the antisymmetric solution doubles the number of maxima when compared with the symmetric solution. Quite remarkably, if we continue with the next magic angle, the parity changes to an odd magic angle ($\alpha_9 = 12.855$), with $\mu_{\alpha} = +1$. Note that, in Fig. 8, the situation is reversed: Now ψ_+ has the double of peaks when compared with ψ_- . The localization centers of ψ_+ and ψ_- are interchanged when compared with α_8 .

Observe how, in both Figs. 7 and 8, magenta dashed lines indicate moiré unit cells, while the supercell here is 3×3 bigger, as the pseudomagnetic potentials define a bigger magnetic unit cell [28]. This bigger period is seen in the coupling potential as $U(\mathbf{r} + \mathbf{a}_{1,2}) = e^{-i\phi}U(\mathbf{r})$; thus, this requires a translation of $3\mathbf{a}_{1,2}$ to recover the crystal periodicity and a phase factor $e^{3i\phi} = 1$. In such a bigger unit cell, the potential is periodic and in fact leads to the quantization rule for the magic angles [28]. The 3×3 unit cells are essential to clearly understand the inversion symmetries of the wave functions as, if only one unit moiré cell is used, the extra phases make the interpretation very difficult.

Our numerical results indicate distinct localization regions for ψ_+ and ψ_- , suggesting that, in Eq. (23), each term can be separately set to zero to satisfy the equation, owing to the strong confinement. Thus, as a solution, we propose that Eq. (23) can be decoupled into

$$[-\nabla^2 + \alpha^2 \mathbf{A}^2 - i\mu_{\alpha}\alpha(-2i\mathcal{A}_{\mp} \cdot \nabla + \nabla \times \mathcal{A}_{\mp})]\psi_{\pm} \approx 0, \quad (24)$$

$$[\alpha^2 \Delta - i\mu_{\alpha}\alpha(-2i\mathcal{A}_{\pm} \cdot \nabla + \nabla \times \mathcal{A}_{\pm})]\psi_{\mp} \approx 0. \quad (25)$$

As explained in Appendix B, by using Eqs. (24) and (25), it can be proved that the following equation is obtained:

$$[-\nabla^2 + \alpha^2 \mathbf{A}^2(\mathbf{r}) - \alpha^2 \Delta(\mathbf{r})]\psi_{\pm} \approx 0, \quad (26)$$

where in Eq. (26), it is supposed $\alpha \rightarrow \infty$, and thus, $\nabla \times \mathcal{A}_{\pm}(\mathbf{r}) \rightarrow 0$ is negligible, as it scales as α . This indeed supports the use of well-defined parity wave functions as was done in a previous work [28].

As is seen in Eq. (26), the potential $\mathbf{A}^2(\mathbf{r}) - \Delta(\mathbf{r})$ governs the electronic localization behavior in the asymptotic limit $\alpha \rightarrow \infty$. However, note that taking $\mathbf{r} \rightarrow -\mathbf{r}$ in Eq. (26) changes the sign of $\Delta(-\mathbf{r}) = -\Delta(\mathbf{r})$ while keeping invariant the other terms. This property allows for the decoupling of the symmetric and antisymmetric potentials as

$$[-\nabla^2 + \alpha^2 \mathbf{A}^2(\mathbf{r})]\psi_{\pm} \approx 0, \quad \Delta(\mathbf{r})\psi_{\pm} \approx 0. \quad (27)$$

To satisfy the second of the previous equations, we must have $\Delta(\mathbf{r}) \approx 0$ in regions where $\psi_{\pm} \neq 0$. Figure 9(a) confirms numerically that such condition is correct, i.e., wave functions are localized in the lines for which $\Delta(\mathbf{r}) = 0$. Moreover, this implies that localization occurs whenever $[A_x, A_y] = 0$. Therefore, locally, the system is Abelian.

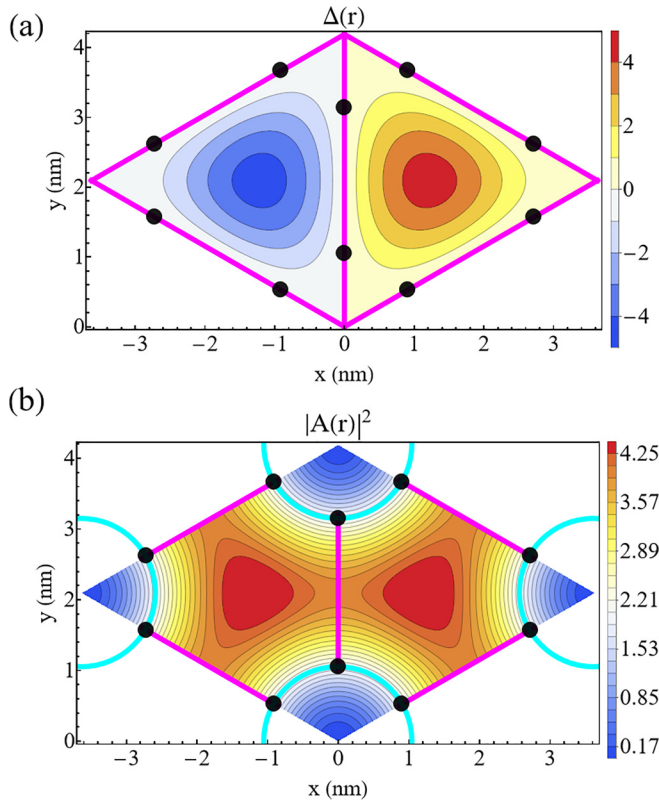


FIG. 9. Confinement spots and potentials in the unit cell defined using the vectors \mathbf{a}_1 and \mathbf{a}_2 . (a) Antisymmetric potential $\Delta(\mathbf{r})$ and (b) symmetric potential $A^2(\mathbf{r})$. The black points are the localization centers of the electronic zero-mode wave function. In the antisymmetric potential $\Delta(\mathbf{r})$, magenta lines indicate angular confinement directions where, locally, the non-Abelian commutator is zero $\Delta(\pm 1.047\mathbf{q}_v) = i[A_x, A_y] = 0$, the directions are defined by vectors $\pm 1.047\mathbf{q}_v$. The symmetric potential $A^2(\mathbf{r})$ is also important because it tells us some information related to radial confinement. In (b), cyan circles have a radius 1.047, and black points lie around these circles. More importantly, $\mathbf{R} \approx \pm 1.047\mathbf{q}_v$ corresponds to special points restricted by the angular confinement directions of $\Delta(\mathbf{r})$. These special points are also related to tunneling paths (magenta lines) that are energetically favorable and connect electronic density centers by a saddle point.

Energetically, this is explained by the fact that, in H^2 , $E = 0$ is the ground state. Therefore, the ground state will minimize the expected value of $\Delta(\mathbf{r})$, and this is done by angular confinement in regions where $\Delta(\mathbf{r}) \approx 0$. For regions where $\Delta(\mathbf{r}) \neq 0$, there is an extra energetic cost. However, such angular confinement can only be reached as $\alpha \rightarrow \infty$, once the wave functions are so well confined that overlaps are small, allowing us to separate it into regions with different parities, as shown in Figs. 7 and 8.

Note that $\Delta(\mathbf{r}) \approx 0$ does not imply the vanishing of the pseudomagnetic field at such symmetric lines. In fact, it is the opposite; the pseudomagnetic field remains more or less constant while avoiding the nodes. To comprehend the localization of the Gaussian centers, an investigation of the role of angular momenta is necessary.

As shown in Appendix A, the positions where $\Delta(\mathbf{r}) = 0$ occur at high-symmetry directions, so the localization centers,

for the vertex at the origin, will have numerically found positions near

$$\mathbf{R} \approx \pm R\mathbf{q}_v, \quad (28)$$

where $R = 1.047\dots$ is the magnitude of \mathbf{R} . It gives the radial distance of the maximum to the vertex of the cell. Its value is determined from the condition $[-\nabla^2 + \alpha^2 A^2(\mathbf{r})]\psi_{\pm} \approx 0$. Also, the angular part of the wave function will behave closely to $\cos(3m\theta)$, in agreement with the results obtained in a previous work, where we showed that the angular momentum becomes quantized by $3m$, as also suggested by Figs. 7 and 8. In Fig. 9(b), we present $A^2(\mathbf{r})$. We observe that there are no relevant features that give any indication of a possible confinement. However, such confinement arises when we consider the angular momentum. This is best seen by working near the origin and using polar coordinates. The first equation in Eq. (27) now looks as

$$-\left(\frac{\partial^2 \psi_{\pm}}{\partial r^2} + \frac{1}{r} \frac{\partial \psi_{\pm}}{\partial r} + \frac{1}{r^2} \frac{\partial^2 \psi_{\pm}}{\partial \theta^2}\right) + \alpha^2 A^2(\mathbf{r})\psi_{\pm} = 0. \quad (29)$$

As the third term in the Laplacian is the angular momentum, we see that an effective potential appears which contains the moiré symmetric potential part plus the centrifugal barrier, which is a result of the orbital motion of the electron. Elsewhere, it was shown [28] that the magic angle is given by $\alpha_m \approx 3m/2$, and asymptotically, $L_z \psi_{\pm} \approx m\psi_{\pm}$. Also, we can discard the second term of the Laplacian, as derivatives scale with α inside the boundary layer of the equation [28]. We obtain that

$$-\frac{\partial^2 \psi_{\pm}}{\partial r^2} + \frac{9}{4}m^2 \left[\frac{1}{r^2} + A^2(\mathbf{r}) \right] \psi_{\pm} \approx 0. \quad (30)$$

A bound state will appear if the effective potential has a minimum. As we also have the condition on the angular part that confines electrons in certain directions, here, we will discuss the minimum that results in the y direction. This is seen in Fig. 10, where we plot the potentials $A^2(0, y)$, $1/y^2$ and the effective one $V_{\text{eff}} = 1/y^2 + A^2(0, y)$. As seen in the plot, the minima are close to the numerically found limiting confinement centers for the wave functions, indicated in Fig. 10 by vertical lines. The minimum can be found from

$$\left(\frac{dV_{\text{eff}}}{dy}\right)_{y=R} = -\frac{2}{R^3} + 3 \sin\left(\frac{3R}{2}\right) = 0. \quad (31)$$

We found numerically that the minimum is approximately $R \approx 0.88$. Notice that the obtained minimum is shifted with respect to the numerical obtained value, i.e., the error is $\Delta R \approx 1.047 - 0.88 \approx 0.16$, which is $\sim 15\%$. The reason is that we made several strong approximations like neglecting overlaps between localization centers, the correct shape of the angular part which introduces a factor in the angular momentum, etc. Around the localization center, the effective potential can be approximated with a parabola. Therefore, we obtain an effective harmonic oscillator equation:

$$-\frac{\partial^2 \psi_{\pm}}{\partial y^2} + \left(\frac{3m}{2}\right)^2 \left[V_{\text{eff}}(R) + \frac{\omega^2(R)}{2}(y - R)^2 \right] \psi_{\pm} \approx 0, \quad (32)$$

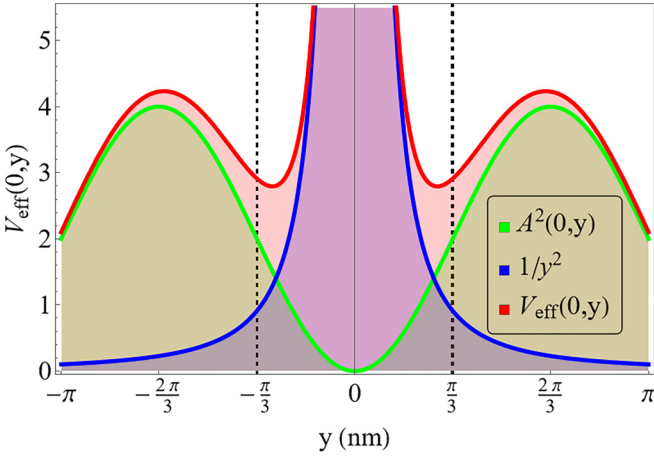


FIG. 10. Effective potential $V_{\text{eff}}(r)$ along the axis $\mathbf{r} = (0, y)$. The blue curve is the function $1/y^2$, while the green curve is $A^2(0, y)$. Electrons are confined in the well around the local minima of the effective potential (red curve) at $R \approx 0.88$. In this plot, we include two dashed vertical lines that indicate the position where the numerically found electronic wave function has its localization center ($R \approx 1.047$) for the limit $\alpha \rightarrow \infty$.

where the frequency is

$$\omega^2(R) = \left[\frac{d^2 V_{\text{eff}}(y)}{dy^2} \right]_{y=R} = \frac{6}{R^4} + \frac{9}{2} \cos\left(\frac{3R}{2}\right). \quad (33)$$

On the other hand, the result from the scaling argument σ has an associated frequency $\omega = 3\alpha$ (see Ref. [28]), as the energy rescales as $1/\alpha^2$. Thus, the scaled frequency is $\omega' = \frac{\omega}{\alpha} = 3$, and so $\omega^2 = 9$, where primes are omitted. Therefore, comparing $\omega^2 = 9$ with $\omega^2(R)$ at $R = 1.047$, we found that $\omega^2(R) \approx 9.489$; hence, the error is $\Delta\omega = \omega^2 - \omega^2(R) \approx 0.489$, which is $\sim 5\%$. For $R \approx 0.88$, the frequency is $\omega^2(R) \approx 11.121$. The error is $\Delta\omega = \omega^2 - \omega^2(R) \approx 2.121$, which is $\sim 19\%$.

The zero mode can thus be interpreted as the ground state of this effective harmonic oscillator with an energy shift determined by $m^2 V_{\text{eff}}(R)$ and guiding center R . Thus, this explains the Gaussian shape for the electronic density discussed in the previous section, and in fact, the degree of similarity of the wave function to a Gaussian is determined by how close the approximation of the effective potential is to a parabola.

We add that, although the pseudomagnetic vanishes along symmetric directions, the wave functions are angular confined in between these lines, precisely in regions where $\Delta(\mathbf{r}) \approx 0$. Therein, the pseudomagnetic field is almost spatially constant and thus behaves as Abelian.

Finally, it is important to remark that our analysis was made for the Γ point. The reason is that such a mode is at the top of the band and thus signals the magic angles whenever its corresponding energy goes to zero [30]. At other \mathbf{k} points, numerical calculations indicate that the wave functions also converge toward the same localization center [30]. This can be easily explained by examining Eq. (14). In the limit $\alpha \rightarrow \infty$, the maxima in reciprocal space satisfy $|\mathbf{K}_{l,n}| = |\mathbf{b}_1 + n\mathbf{b}_2| \gg |\mathbf{k}|$ when l and n are $\gg 1$. Consequently, \mathbf{k} can be neglected in all expressions, leading to the collapse of all \mathbf{k} values into the same equation.

V. RELATIONSHIP WITH THE NON-ABELIAN MAGNETIC QHE AND MAGNETIC MAGIC-ANGLE PARITY ORDER

In this section, we will explore some interesting connections with non-Abelian magnetic fields and the related magnetic energy. For convenience, each of these subjects is presented in separate subsections.

A. Non-Abelian magnetic QHE

We now write the squared Hamiltonian:

$$\begin{aligned} H^2 = & (-\nabla^2 + \mathbf{A}^2)\tau_0 + i\alpha^2[A_x, A_y]\tau_z - 2i\alpha\hat{\mathbf{A}} \cdot \nabla \\ & + \alpha(\partial_x \hat{A}_y - \partial_y \hat{A}_x), \end{aligned} \quad (34)$$

where $\hat{\tau}_j$ (with $j = 1, 2, 3$) is the set of Pauli matrices in the pseudospin-layer degree, and the identity 2 matrix $\hat{\tau}_0$. Moreover, A_x and A_y , and its matrices SU(2) versions \hat{A}_x and \hat{A}_y are defined in Appendix A. Written in such a way, we can identify the Zeeman coupling energy as

$$\begin{aligned} \hat{F}_{xy} = & \partial_x \hat{A}_y - \partial_y \hat{A}_x + i\alpha[\hat{A}_x, \hat{A}_y] \\ = & -\hat{\mathbf{B}} \cdot \hat{\boldsymbol{\tau}} + i\alpha[\hat{A}_x, \hat{A}_y], \end{aligned} \quad (35)$$

where upper hats represent matrices. For convenience, we rescale the spatial coordinates as $\mathbf{r}' = \mathbf{r}/\alpha$, from which $\nabla' = (\alpha\nabla)$ and $(\nabla')^2 = (\alpha\nabla)^2$. The rescaled position Hamiltonian is

$$\begin{aligned} \left(\frac{H}{\alpha}\right)^2 = & \left[-\nabla'^2 + \mathbf{A}'^2\left(\frac{\mathbf{r}'}{\alpha}\right)\right]\tau_0 + i\left[A_x\left(\frac{\mathbf{r}'}{\alpha}\right), A_y\left(\frac{\mathbf{r}'}{\alpha}\right)\right]\tau_z \\ & - 2i\hat{\mathbf{A}}\left(\frac{\mathbf{r}'}{\alpha}\right) \cdot \nabla' - \frac{1}{\alpha}\hat{\mathbf{B}}\left(\frac{\mathbf{r}'}{\alpha}\right) \cdot \hat{\boldsymbol{\tau}}, \end{aligned} \quad (36)$$

where now the primes are dropped. As explained in Appendix A, the strong confinement of electrons allows us to suppose an almost uniform magnetic field. This is also seen in the effective Eq. (30). Therefore, we can write $\mathbf{A} \cdot \hat{\mathbf{p}} \approx -\mathbf{B} \cdot \hat{\mathbf{L}}$, where $\hat{\mathbf{L}}$ is the total angular momentum. Under this simplification, the rescaled Hamiltonian is

$$\begin{aligned} \hat{H}^2 = & \overbrace{\left[-\nabla^2 + \mathbf{A}^2\left(\frac{\mathbf{r}}{\alpha}\right)\right]\tau_0 + i\left[A_x\left(\frac{\mathbf{r}}{\alpha}\right), A_y\left(\frac{\mathbf{r}}{\alpha}\right)\right]\tau_z}^{\text{diagonal energy}} \\ & \underbrace{-\hat{\mathbf{B}}\left(\frac{\mathbf{r}}{\alpha}\right) \cdot \left(2\hat{\mathbf{L}} + \frac{\mathbf{e}_z}{\alpha}\right)}_{\text{off-diagonal energy}}. \end{aligned} \quad (37)$$

Note that only the last term depends on α , and taking the asymptotic limit $\alpha \rightarrow \infty$, we have that the Zeeman energy $-\frac{1}{\alpha}\hat{\mathbf{B}}(\mathbf{r}/\alpha) \cdot \boldsymbol{\tau} \rightarrow 0$. This fact is corroborated in Fig. 11, where it can be observed that, for the first magic angle, the expected value of the Zeeman energy scaled by α is significant. However, the third magic angle is very small ~ 0.1 on the logarithmic scale. Therefore, it is expected to be similarly small for higher magic angles, and neglecting it should not significantly impact the results. Thus, in the asymptotic limit $\alpha \rightarrow \infty$, $2\hat{\mathbf{B}}(\mathbf{r}/\alpha) \cdot \hat{\mathbf{L}} \gg \hat{\mathbf{B}}(\mathbf{r}/\alpha) \cdot \mathbf{e}_z/\alpha$, i.e., $E_{\text{Magnetic}} \gg E_{\text{Zeeman}}$. Hence, the Hamiltonian in this limit can be simplified

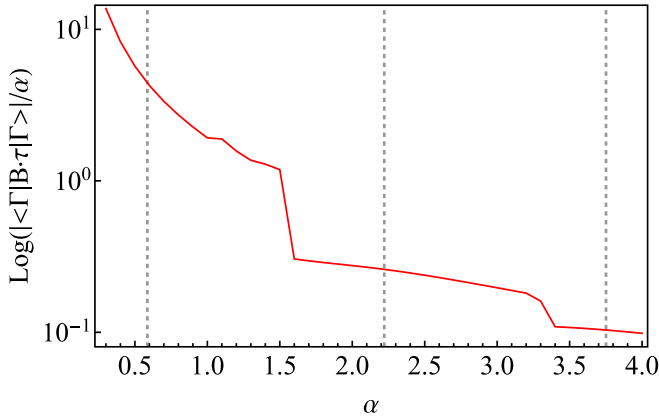


FIG. 11. Zeeman energy $\ln |\langle \Gamma | \mathbf{B} \cdot \hat{\boldsymbol{\tau}} | \Gamma \rangle| / \alpha$ as function of α for the zero-mode wave function at the Γ point. As α increases, the Zeeman energy is quite small, and for higher magic angles, α_8 or α_9 can be negligible. Dashed vertical lines indicate the first three magic angles.

into

$$\hat{H}^2 = \underbrace{\left[\mathbf{p} + \hat{\mathbf{A}}\left(\frac{\mathbf{r}}{\alpha}\right) \right]^2}_{C_3 \text{ magnetic field}} + i \underbrace{\left[A_x\left(\frac{\mathbf{r}}{\alpha}\right), A_y\left(\frac{\mathbf{r}}{\alpha}\right) \right]}_{\text{non-Abelian operator}} \tau_z, \quad (38)$$

where $\hat{H}^2 = (H/\alpha)^2$ and $\mathbf{p} = -i\nabla$ is the canonical momentum operator. Accordingly, \hat{H}^2 is expected to have a non-Abelian QHE.

B. Magnetic parity energy and magic-angle order

Let us discuss how the magic-angle order parity enters the orbital magnetic energy related to the angular momentum chirality. To understand this, we start by writing the zero-mode equation $H^2\psi(\mathbf{r}) = 0$ together with Eq. (37) at the Γ point, where $\psi_2(\mathbf{r}) = i\mu_\alpha\psi_1(-\mathbf{r})$. Using the results of Appendix A in the limit $\alpha \rightarrow \infty$, such that the wave function at the Γ point is strongly confined, we obtain

$$\left[-\nabla^2 + \mathbf{A}^2\left(\frac{\mathbf{r}}{\alpha}\right) + \Delta\left(\frac{\mathbf{r}}{\alpha}\right) \right] \psi_1(\mathbf{r}) - 2i\mu_\alpha \mathbf{B}\left(\frac{\mathbf{r}}{\alpha}\right) \cdot \hat{\mathbf{L}} \psi_1(-\mathbf{r}) = 0. \quad (39)$$

The corresponding expected values over the zero-mode wave function at the Γ point are

$$\langle \Gamma | T\left(\frac{\mathbf{r}}{\alpha}\right) | \Gamma \rangle + \langle \Gamma | \mathbf{A}^2\left(\frac{\mathbf{r}}{\alpha}\right) | \Gamma \rangle - 2i\mu_\alpha \langle \Gamma | \mathbf{B}\left(\frac{\mathbf{r}}{\alpha}\right) \cdot \hat{\mathbf{L}} | \Gamma \rangle = 0, \quad (40)$$

where $T(\mathbf{r}/\alpha)$ is the kinetic energy, i.e., minus the Laplacian, and we have used that the antisymmetric potential is canceled inside the unit cell $\langle \Gamma | \Delta(\mathbf{r}/\alpha) | \Gamma \rangle = 0$ [see Fig. 9(a)]. At magic angles, we can use the energy equipartition found in a previous work [30], from where $\langle \Gamma | T(\mathbf{r}/\alpha) | \Gamma \rangle = \langle \Gamma | \mathbf{A}^2(\mathbf{r}/\alpha) | \Gamma \rangle$. Thus,

$$\langle \Gamma | \mathbf{A}^2\left(\frac{\mathbf{r}}{\alpha}\right) | \Gamma \rangle - i\mu_\alpha \langle \Gamma | \mathbf{B}\left(\frac{\mathbf{r}}{\alpha}\right) \cdot \hat{\mathbf{L}} | \Gamma \rangle = 0, \quad (41)$$

where it is important to note that

$$\begin{aligned} -i\mu_\alpha \mathbf{B}\left(\frac{\mathbf{r}}{\alpha}\right) \cdot \hat{\mathbf{L}} &= -i \sum_{\nu} (-i) \exp\left(-i\mathbf{q}_\nu \cdot \frac{\mathbf{r}}{\alpha}\right) \\ &\quad \times \mathbf{e}_z \cdot (\mu_\alpha \mathbf{q}_\nu \times \hat{\mathbf{p}}) \\ &= - \sum_{\nu} \exp\left(-i\mathbf{q}_\nu \cdot \frac{\mathbf{r}}{\alpha}\right) \mathbf{e}_z \cdot (\mu_\alpha \hat{\mathbf{L}}_\nu) \\ &= - \sum_{\nu} \mathbf{B}_\nu\left(\frac{\mathbf{r}}{\alpha}\right) \cdot (\mu_\alpha \hat{\mathbf{L}}_\nu), \end{aligned} \quad (42)$$

where $\mathbf{B}_\nu(\pm\mathbf{r}/\alpha) = \pm i \exp(\pm i\mathbf{q}_\nu \cdot \mathbf{r}/\alpha)$, and we defined

$$\hat{\mathbf{M}}_\nu = \mu_\alpha \hat{\mathbf{L}}_\nu \quad (43)$$

as the pseudomagnetic orbital momentum at the direction ν , with $\hat{\mathbf{L}}_\nu = \mathbf{q}_\nu \times \hat{\mathbf{p}}$ a kind of angular momentum operator. We can understand its origin as a consequence of the strong confinement as, in the angular momentum $\hat{\mathbf{L}}_z = \mathbf{r} \times \mathbf{p}$, \mathbf{r} takes only values different from zero at $\mathbf{r} \approx \mathbf{q}_\nu$. Therefore, we can interpret $\hat{\mathbf{L}}_\nu$ as the contribution to the angular momentum of each confinement center, as these centers are not in the origin of coordinates. Such an observation was empirically made by analyzing the numerical data in a previous paper [28]. In the asymptotic limit $\alpha \rightarrow \infty$, we have that [30] $\langle \Gamma | \mathbf{A}^2(\mathbf{r}/\alpha) | \Gamma \rangle \rightarrow 1$, from which

$$\begin{aligned} 1 - \int d^2\mathbf{r} \psi_1^\dagger(\mathbf{r}) \sum_{\nu} \exp\left(-i\mathbf{q}_\nu \cdot \frac{\mathbf{r}}{\alpha}\right) \mathbf{e}_z \\ \times (\mu_\alpha \hat{\mathbf{L}}_\nu) \psi_1(-\mathbf{r}) = 0; \end{aligned} \quad (44)$$

therefore,

$$\begin{aligned} 1 - \mu_\alpha \mathbf{e}_z \cdot \sum_{\nu} \int d^2\mathbf{r} \psi_1^\dagger(\mathbf{r}) \exp\left(-i\mathbf{q}_\nu \cdot \frac{\mathbf{r}}{\alpha}\right) \hat{\mathbf{L}}_\nu \psi_1(-\mathbf{r}) \\ = 1 - \mu_\alpha |\mathbf{e}_z|^2 \sum_{\nu} \left(\frac{\mu_\alpha}{3}\right) \\ = 1 - \mu_\alpha^2 = 0, \end{aligned} \quad (45)$$

where natural units $e = \hbar = 1$ and rescaled energies $1/\alpha^2$ are used, normalized over the moiré unit cell area. Each contribution of plane waves in the sum contributes $\frac{1}{3}$ to the integral, i.e.,

$$\frac{1}{\alpha A_M} \langle \psi_1(\mathbf{r}) | \mathbf{B}_\nu\left(\frac{\mathbf{r}}{\alpha}\right) \cdot \hat{\mathbf{L}}_\nu | \psi_1(-\mathbf{r}) \rangle = \frac{\mu_\alpha}{3}, \quad (46)$$

where $A_M = 8\pi^2/(3\sqrt{3})$ is the normalized moiré unit cell area. This proves that parity and the three directional components of the angular momentum are essential to satisfy the magic-angle condition. Moreover, Eq. (43) indicates that the parity is related to the chirality of the magnetic energy.

To corroborate the chirality of the magnetic energy, in Fig. 12, we plot $\langle \Gamma | \mathbf{B}(\mathbf{r}/\alpha) \cdot \hat{\mathbf{L}} | \Gamma \rangle / \alpha$ vs α at the Γ point, as obtained from the numerical data of the wave function, by using techniques described in previous works [28,30]. In the y axis, this magnetic energy jumps from $\mu_\alpha = +1 \rightarrow -1$ or vice versa. Because we rescaled the coordinates, the energy is also rescaled as $E^2 = (E/\alpha)^2$, and thus, the result does not depend on α .

Figure 12 also shows the relation between $\mu_\alpha = +1$ counterclockwise rotation (red arrows) and $\mu_\alpha = -1$ clockwise

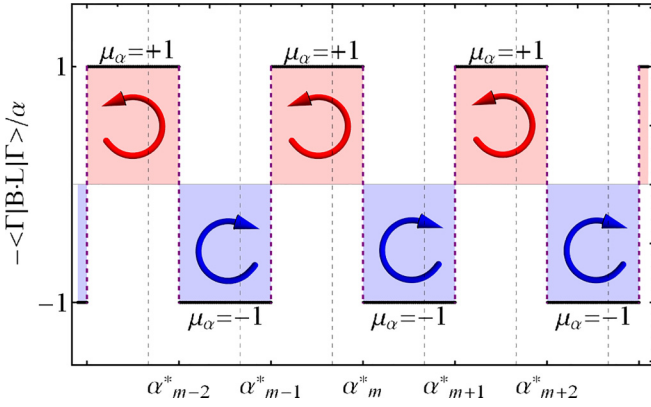


FIG. 12. Orbital magnetic energy $-\langle\Gamma|\mathbf{B}\cdot\hat{\mathbf{L}}|\Gamma\rangle/\alpha$ as a function of α in the limit $\alpha \rightarrow \infty$ for the zero-mode wave function at the Γ point, obtained from the numerical data of the wave function as in previous works [28,30]. Vertical dashed lines (black) indicate magic angles. The red and blue arrows indicate the magnetic orbital rotation, $\mu_\alpha = +1$ is counter-clockwise, and $\mu_\alpha = -1$ is clockwise rotation. Here are considered scaled coordinates $\mathbf{r}' = \mathbf{r}/\alpha$, when $\alpha \rightarrow \infty$ approximately $\alpha \approx 3m$, where $m \gg 1$ is the order of the magic angle, and $-\langle\Gamma|\mathbf{B}(\mathbf{r}/\alpha)\cdot\hat{\mathbf{L}}|\Gamma\rangle/\alpha \approx \mu_\alpha$. The transition points α_m^* , in between magic angles α_m and α_{m+1} , occur when the flat band touches the upper band generating a transition and consequently changes the magnetic orbital orientation. These touching points relate to the magic angle recurrence. Similarly, in the other layer, $\mathbf{B}(\mathbf{r}/\alpha) \rightarrow \mathbf{B}(-\mathbf{r}/\alpha)$.

rotation (blue arrows) as the z component rotation of the magnetic angular momentum. The values α_m^* indicate the intermediate values between magic angles α_m and α_{m+1} . At these special values, the gap closes, and the zero mode hybridizes with its neighbor upper band, changing the chirality of the angular momentum.

Thus, an important characteristic of TBG is the gap closing in between magic angles due to the hybridization of the lowest band with its neighbor upper band. This is a crucial condition because it is a transition that changes the chirality of the angular momentum and the magic-angle order parity $\mu_\alpha = \pm 1$. At the same time, on each gap closing appears new quanta of angular momentum, and consequently, the magnetic angular momentum increases as $\alpha \rightarrow \infty$.

So far, in this analysis, it is clear that parity of the wave function and the sign μ_α play a crucial role in the energetic balance for magic-angle flat bands; nevertheless, only at higher magic angles does the wave function reach a purely symmetric or antisymmetric solution, and in this way, the angular momentum quantum number and the magic-angle order parity govern the physics behind flat bands.

VI. COMPETITION BETWEEN NON-ABELIAN AND ABELIAN FIELDS

The cTBG model is quite interesting and exhibits remarkable properties due to its non-Abelian nature introduced by the coupling potential $U(\mathbf{r})$ between layers [75,76]. In fact, flat bands and superconductivity in TBG are consequences of the underlying pseudomagnetic fields generated by the twist angle. However, what if we could tune non-Abelian fields to

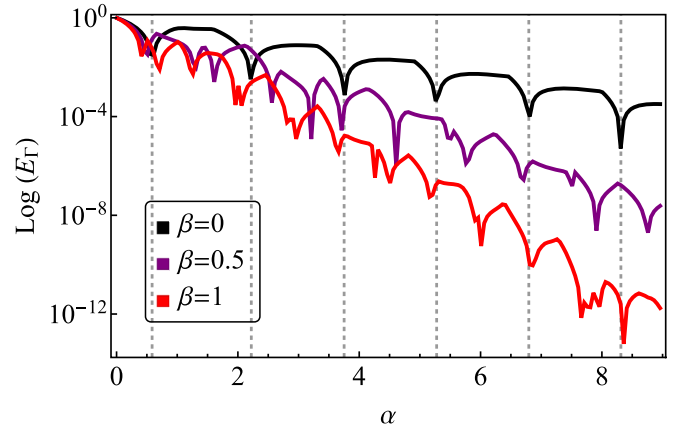


FIG. 13. Energy E_Γ , in log scale, as a function of α at the Γ point. The β parameter transforms the original chiral model with a non-Abelian nature to an Abelian system. In the curve $\beta = 1$, the off-diagonal term is proportional to $\hat{\tau}_x$, and there is no well-defined $\frac{3}{2}$ magic angle recurrence as for the chiral twisted bilayer graphene (cTBG; $\beta = 0$). Vertical lines indicate magic angles.

become Abelian using an artificial parameter? How would this modification affect the periodicity and quantization of magic angles? To explore this effect, we can define a new coupling potential as follows:

$$U_\beta(\mathbf{r}) = U(\mathbf{r}) + \beta U(-\mathbf{r}), \quad (47)$$

where β is the artificial parameter that controls the non-Abelian nature of TBG. Suppose that $\beta \in [0, 1]$; with $\beta = 0$, we recovered the cTBG case, while $\beta = 1$ is presumably an Abelian case. Using this new potential we can write a new Hamiltonian as

$$\mathcal{H}_\beta = \begin{bmatrix} 0 & D_\beta^*(-\mathbf{r}) \\ D_\beta(\mathbf{r}) & 0 \end{bmatrix}, \quad (48)$$

where the zero-mode operator is

$$D_\beta(\mathbf{r}) = \begin{bmatrix} -i\bar{\partial} & \alpha U_\beta(\mathbf{r}) \\ \alpha U_\beta(-\mathbf{r}) & -i\bar{\partial} \end{bmatrix}. \quad (49)$$

The Abelian case $\beta = 1$ gives

$$D_1(\mathbf{r}) = \begin{pmatrix} -i\bar{\partial} & 0 \\ 0 & -i\bar{\partial} \end{pmatrix} + \begin{bmatrix} 0 & \alpha U_1(\mathbf{r}) \\ \alpha U_1(-\mathbf{r}) & 0 \end{bmatrix}; \quad (50)$$

however, $U_1(-\mathbf{r}) = U_1(\mathbf{r})$, so

$$D_1(\mathbf{r}) = -i\bar{\partial}\hat{\tau}_0 + \alpha U_1(\mathbf{r})\hat{\tau}_x, \quad (51)$$

where $U_1(\mathbf{r}) = 2 \sum_\nu \exp[i(\nu - 1)\phi] \cos(\mathbf{q}_\nu \cdot \mathbf{r})$ is the symmetric coupling potential. Now it is clear from these expressions that the vector potential commute, and the initial $SU(2)$ gauge field changes to a $U(1)$ field.

Figure 13 shows the zero energy mode in log scale as a function of α for different values of β . The non-Abelian structure of cTBG clearly plays a vital role in magic-angle recurrence. Interestingly, even at $\beta = 1$, it exhibits a decaying behavior; however, it does not have a well-defined $\frac{3}{2}$ magic-angle recurrence rule. Furthermore, when $\beta = 0 \rightarrow 1$, the band gap has an extra squeezing, as $\Delta \sim \Delta_\alpha e^{-C\beta}$, where C is a scaling constant, and Δ_α is the original band gap of cTBG independent of the parameter β . A rigorous mathematical

study on the exponential decay was recently made by Zworsky *et al.* [77].

Although in this section our primary focus was on how the magic-angle sequences change with the alteration of the non-Abelian nature of the potential, one can envision some experimental realizations of such a potential. The simplest approach is to begin with twisted trilayer graphene and then pull away one layer while maintaining the other two layers at the same distance. Consequently, this system represents weakly perturbed TBG with a potential that is like that described in Eq. (47).

VII. CONCLUSIONS

In this paper, we studied TBG at small magic angles to understand the properties of the electron wave functions. We corroborated that zero-mode states converge into coherent Landau states with minimal dispersion. In reciprocal space, they have the same shape (almost Gaussian) as in real space but with inverted parameters. These coherent states exhibit minimal dispersion with a standard deviation in reciprocal space of $\sigma_k = \sqrt{3\alpha/2\pi}$ as α approaches infinity.

Importantly, as α approaches infinity, the zero-mode equation decouples into its symmetric and antisymmetric components. Exploiting this property and the squared Hamiltonian, we have elucidated the reason for the confinement of the electronic wave function as α tends to infinity. Specifically, this confinement arises from the interplay between the squared norm of the moiré potential and the quantized orbital motion of electrons, resulting in the formation of a quantum well. Inside this well, an effective harmonic oscillator is identified, giving rise to Landau levels.

As the squared Hamiltonian gives rise to an effective quantum oscillator, we also showed how to relate it with the non-Abelian QHE. Then we defined a magnetic and Zeeman energy. The Zeeman energy is negligible for high-order magic angles, while the magnetic term can be interpreted as orbital magnetic energy with a well-defined chirality. This highlights the important role of the Γ -point wave function parity, as it changes at each gap closing. Finally, we also altered the non-Abelian intrinsic behavior of TBG to see how the $\frac{3}{2}$ quantization rule of flat bands is destroyed by such an artifact. An experimental proposal has been made to observe such an effect.

Therefore, we conclude that the relationship between TBG physics and the QHE is not coincidental. Our recent analytical work on flat bands in graphene without twists has also confirmed such a conclusion in a very clear and concise way [78].

It is worthwhile to add some comments concerning the extension of our results beyond the chiral case studied here. It is now known that Eq. (1) should be augmented with a perturbation Hamiltonian featuring a coupling parameter of the order of $w_0/w_1 \approx 0.7$, where w_0 represents the interlayer coupling at AA stacking regions [29,54]. In this case, squaring Eq. (1) does not yield an effective 2×2 Hamiltonian. Instead, it introduces coupling between two copies of a 2×2 Hamiltonian. However, it is still possible to perform a projection, resulting in a modified effective 2×2 Hamiltonian. This resulting Hamiltonian can be treated by considering w_0/w_1 as

a perturbation parameter, allowing for the calculation of corrections using the wave functions presented in this paper. Our preliminary results, confirmed by numerical simulations, indicate that, for high-order magic angles, the Gaussian density remains conserved, but the localization centers are displaced toward $\mathbf{r} = 0$. The confinement also increases as a result of an additional energy term that emerges in the expression of the effective quantum well. Given its significance, we intend to provide a detailed analysis of the induced corrections in the nonchiral limit in an upcoming work.

Finally, the localization properties discussed in this paper can be experimentally accessed by searching for signatures using scanning tunneling microscopy (STM) and spectroscopy, as described in the study by Liu *et al.* [79]. Therefore, we predict that, for high-order magic angles, the electronic density is shifted away from AA stacking regions due to the centrifugal barrier. This result holds true even when considering nonchiral corrections, as it is an effect of nonzero angular momentum.

ACKNOWLEDGMENTS

This paper was supported by CONAHCyT Project No. 1564464 and UNAM DGAPA Project No. IN101924. Leonardo Navarro is supported by a CONAHCyT Ph.D. scholarship. We thank P. Pantaleon at IMDEA, Madrid, for enlightening discussions and feedback about this project and E. Khalaf at Harvard University (now at Texas University) for valuable comments on the section concerning the artificial potential. The authors acknowledge and express gratitude to Carlos Ernesto Loópez Natarén from Secretaria Técnica de Cómputo y Telecomunicaciones for helping with the high-performance computing infrastructure where we run our calculations and his valuable support.

APPENDIX A: NON-ABELIAN PSEUDOMAGNETIC FIELD AND ANGULAR MOMENTUM

As explained before, electrons in TBG behave like a $SU(2)$ non-Abelian pseudomagnetic vector potential. In matrix notation, it follows that

$$\hat{\mathbf{A}} = (\hat{A}_x, \hat{A}_y), \quad (\text{A1})$$

with $\hat{A}_x = A_{1,x}\hat{\tau}_1 + A_{2,x}\hat{\tau}_2$ and $\hat{A}_y = A_{1,y}\hat{\tau}_1 + A_{2,y}\hat{\tau}_2$, where we used the set of Pauli matrices $\hat{\tau}_j$ (with $j = 1, 2, 3$) in the pseudospin-layer degree and the identity matrix $\hat{\tau}_0$. Explicitly, the components of $\hat{\mathbf{A}}$ are

$$\begin{aligned} A_{1,x} &= \sum_{\nu} \cos(\mathbf{q}_{\nu} \cdot \mathbf{r}) \mathbf{q}_{\nu}^{\perp,x}, \\ A_{2,x} &= \sum_{\nu} \cos(\mathbf{q}_{\nu} \cdot \mathbf{r}) \mathbf{q}_{\nu}^{\perp,y}, \\ A_{1,y} &= \sum_{\nu} \sin(\mathbf{q}_{\nu} \cdot \mathbf{r}) \mathbf{q}_{\nu}^{\perp,x}, \\ A_{2,y} &= \sum_{\nu} \sin(\mathbf{q}_{\nu} \cdot \mathbf{r}) \mathbf{q}_{\nu}^{\perp,y}. \end{aligned} \quad (\text{A2})$$

Note that $\hat{\mathbf{A}}$ is non-Abelian, as follows from the fact that $[\hat{A}_{\nu}, \hat{A}_{\eta}] \neq 0$ for $\nu \neq \eta$. On the other hand, the off-diagonal

terms of H^2 related to the angular momentum and interlayer currents [30] have two contributions:

$$\nabla \times \mathbf{A}_\pm = \mathbf{B}_\pm, \quad (\text{A3})$$

where \mathbf{B}_\pm represents a pseudomagnetic field, while the other term is

$$-2i\mathbf{A}_\pm \cdot \nabla = -2\mathbf{B}_\pm \cdot \hat{\mathbf{L}}. \quad (\text{A4})$$

Explicitly, we have that

$$\mathbf{A}(\pm\mathbf{r}) \cdot \hat{\mathbf{p}} = -\sum_\nu B_\nu(\pm\mathbf{r})\mathbf{e}_z \cdot (\mathbf{q}_\nu \times \hat{\mathbf{p}}), \quad (\text{A5})$$

where it is convenient to define $\mathbf{q}_\nu \times \hat{\mathbf{p}} = \hat{\mathbf{L}}_\nu$ as an operator similar to the angular momentum at the direction ν , defined by the reciprocal vectors \mathbf{q}_ν . We can interpret $\hat{\mathbf{L}}_\nu$ as the contribution to the angular momentum of each confinement center as $\mathbf{r} \approx \mathbf{q}_\nu$. Accordingly, we can re-express the last relation in a compact form as

$$\mathbf{A}(\pm\mathbf{r}) \cdot \hat{\mathbf{p}} = -\sum_\nu \mathbf{B}_\nu(\pm\mathbf{r}) \cdot \hat{\mathbf{L}}_\nu, \quad (\text{A6})$$

where $\mathbf{A}(\pm\mathbf{r}) = \sum_\nu \exp(\pm i\mathbf{q}_\nu \cdot \mathbf{r})\mathbf{q}_\nu^\perp$, with $\mathbf{q}_\nu^\perp = \mathbf{q}_\nu \times \mathbf{e}_z$. The well-known relation $\mathbf{A} \cdot \hat{\mathbf{p}} = -\mathbf{B} \cdot \hat{\mathbf{L}}$ is used here and comes from a uniform and symmetric gauge magnetic vector potential which can be expressed as $\mathbf{A} = -\frac{1}{2}\mathbf{r} \times \mathbf{B}$, where \mathbf{r}

is the position vector and \mathbf{B} is the magnetic field. It can be used due to the confinement nature of the wave function which allows us to suppose a local uniform magnetic field in the spirit of Eq. (32).

Clearly, we need to recognize the differences in cTBG compared with the conventional QHE in a radial symmetric potential, i.e., cTBG has C_3 symmetry and the periodicity of the superlattice. Moreover, the pseudomagnetic fields are position dependent and therefore spatially inhomogeneous. Surprisingly, despite these differences, cTBG satisfies this magnetic property due to the local Abelian features induced by confinement.

Hence, Eq. (A6) is analogous to the relation $\mathbf{A} \cdot \hat{\mathbf{p}} = -\mathbf{B} \cdot \hat{\mathbf{L}}$ used in symmetric gauge magnetic fields. Note in Eq. (A6) that the direct product between the pseudomagnetic field and the angular momentum is a superposition of three plane waves. This off-diagonal operator is quite important for engineering flat bands at magic angles and, moreover, introduces the magic-angle order parity in the energy equipartition rule balance for flat bands.

On the other hand, the squared TBG system is a 2×2 matrix operator where the layer degree of freedom introduces $SU(2)$ Pauli matrices $\boldsymbol{\tau}$, and in this manner, it is convenient to re-express the off-diagonal operator using matrices to consider the effect of both layers, from which it follows that

$$-2i\hat{\mathbf{A}} \cdot \nabla = \begin{bmatrix} 0 & 2\sum_\nu \exp(-i\mathbf{q}_\nu \cdot \mathbf{r})\mathbf{q}_\nu^\perp \cdot \hat{\mathbf{p}} \\ 2\sum_\nu \exp(i\mathbf{q}_\nu \cdot \mathbf{r})\mathbf{q}_\nu^\perp \cdot \hat{\mathbf{p}} & 0 \end{bmatrix}, \quad (\text{A7})$$

and since $\hat{\mathbf{A}} \cdot \hat{\mathbf{p}} \approx -\hat{\mathbf{B}} \cdot \hat{\mathbf{L}}$, it follows that

$$\begin{aligned} -2i\hat{\mathbf{A}} \cdot \nabla &= \begin{bmatrix} 0 & 2\mathbf{A}(\mathbf{r}) \cdot \hat{\mathbf{p}} \\ 2\mathbf{A}(-\mathbf{r}) \cdot \hat{\mathbf{p}} & 0 \end{bmatrix} \\ &= 2 \begin{bmatrix} 0 & -\mathbf{B}(\mathbf{r}) \cdot \hat{\mathbf{L}} \\ -\mathbf{B}(-\mathbf{r}) \cdot \hat{\mathbf{L}} & 0 \end{bmatrix}. \end{aligned} \quad (\text{A8})$$

This operator is responsible for coupling the layers with pseudomagnetic potentials $B(\mathbf{r})$ (layer 1) and $B(-\mathbf{r})$ (layer 2). This matrix form gives us more insight into the non-Abelian nature of the pseudomagnetic potentials related to the $SU(2)$ layer degree of freedom.

APPENDIX B: SYMMETRIZED ZERO-MODE EQUATION AT THE ASYMPTOTIC LIMIT $\alpha \rightarrow \infty$

As was mentioned in Sec. IV, at the asymptotic limit, the zero-mode equation is decoupled into two separate equations as follows:

$$[-\nabla^2 + \alpha^2 \mathbf{A}^2 - i\mu_\alpha \alpha (-2i\mathcal{A}_\mp \cdot \nabla + \nabla \times \mathcal{A}_\mp)]\psi_\pm \approx 0, \quad (\text{B1})$$

$$[\alpha^2 \Delta - i\mu_\alpha \alpha (-2i\mathcal{A}_\pm \cdot \nabla + \nabla \times \mathcal{A}_\pm)]\psi_\mp \approx 0, \quad (\text{B2})$$

from which, if we consider scaling of the spatial coordinates as $\mathbf{r}' = \mathbf{r}/\alpha$, and therefore, $\nabla' = (\alpha\nabla)$ and $(\nabla')^2 = (\alpha\nabla)^2$, it

follows that energy scales proportional to α^2 ; thus, Eqs. (B1) and (B2) change as

$$[-\nabla^2 + \mathbf{A}^2\left(\frac{\mathbf{r}}{\alpha}\right) - 2\mu_\alpha \mathcal{A}_\mp\left(\frac{\mathbf{r}}{\alpha}\right) \cdot \nabla]\psi_\pm \approx 0, \quad (\text{B3})$$

$$\left[\Delta\left(\frac{\mathbf{r}}{\alpha}\right) - 2\mu_\alpha \mathcal{A}_\pm\left(\frac{\mathbf{r}}{\alpha}\right) \cdot \nabla\right]\psi_\mp \approx 0, \quad (\text{B4})$$

where the term $\nabla \times \mathcal{A}_\pm(\mathbf{r}/\alpha) = \frac{1}{\alpha}\mathcal{B}_\pm \rightarrow 0$, as $\alpha \rightarrow \infty$. From Eq. (B4), it follows that

$$\Delta\left(\frac{\mathbf{r}}{\alpha}\right)\psi_\mp = 2\mu_\alpha \mathcal{A}_\pm\left(\frac{\mathbf{r}}{\alpha}\right) \cdot \nabla\psi_\mp; \quad (\text{B5})$$

thus, substituting Eq. (B5) into Eq. (B3), it is easy to show that

$$[-\nabla^2 + \mathbf{A}^2\left(\frac{\mathbf{r}}{\alpha}\right) - \Delta\left(\frac{\mathbf{r}}{\alpha}\right)]\psi_\pm \approx 0. \quad (\text{B6})$$

From this last expression, it is clear that we can decouple into two separate equations:

$$[-\nabla^2 + \mathbf{A}^2\left(\frac{\mathbf{r}}{\alpha}\right)]\psi_\pm \approx 0, \quad (\text{B7})$$

and

$$\Delta\left(\frac{\mathbf{r}}{\alpha}\right)\psi_\pm \approx 0. \quad (\text{B8})$$

These equations give the localization behavior in the asymptotic limit $\alpha \rightarrow \infty$. Both Eqs. (B7) and (B8) give information related to the radial and angular confinement position,

respectively. The angular directions are defined by $\Delta(\mathbf{r}) = 0$, giving confinement paths along the unit vectors $\pm\mathbf{q}_v$; this is analogous to saying that $[A_x, A_y] = 0$; therefore, the electronic

wave function is locally Abelian. In this manner, cTBG can be interpreted at the asymptotic limit $\alpha \rightarrow \infty$ as an effective quasi-1D system along these preferential directions.

-
- [1] Y. Cao, V. Fatemi, S. Fang, K. Watanabe, T. Taniguchi, E. Kaxiras, and P. Jarillo-Herrero, *Nature (London)* **556**, 43 (2018).
 - [2] J. M. Park, Y. Cao, K. Watanabe, T. Taniguchi, and P. Jarillo-Herrero, *Nature (London)* **590**, 249 (2021).
 - [3] Z.-D. Song and B. A. Bernevig, *Phys. Rev. Lett.* **129**, 047601 (2022).
 - [4] C.-C. Liu, L.-D. Zhang, W.-Q. Chen, and F. Yang, *Phys. Rev. Lett.* **121**, 217001 (2018).
 - [5] F. Wu, A. H. MacDonald, and I. Martin, *Phys. Rev. Lett.* **121**, 257001 (2018).
 - [6] M. Fidrysiak, M. Zegrodnik, and J. Spałek, *Phys. Rev. B* **98**, 085436 (2018).
 - [7] F. Wu, *Phys. Rev. B* **99**, 195114 (2019).
 - [8] M. Yankowitz, S. Chen, H. Polshyn, Y. Zhang, K. Watanabe, T. Taniguchi, D. Graf, A. F. Young, and C. R. Dean, *Science* **363**, 1059 (2019).
 - [9] Y.-Z. You and A. Vishwanath, *npj Quantum Mater.* **4**, 16 (2019).
 - [10] B. Roy and V. Juričić, *Phys. Rev. B* **99**, 121407(R) (2019).
 - [11] A. Kerelsky, L. McGilly, D. M. Kennes, L. Xian, M. Yankowitz, S. Chen, K. Watanabe, T. Taniguchi, J. Hone, C. Dean *et al.*, *Nature (London)* **572**, 95 (2019).
 - [12] A. Uri, S. Grover, Y. Cao, J. Á. A. Crosse, K. Bagani, D. Rodan-Legrain, Y. Myasoedov, K. Watanabe, T. Taniguchi, P. Moon *et al.*, *Nature (London)* **581**, 47 (2020).
 - [13] S. Onari and H. Kontani, *Phys. Rev. Lett.* **128**, 066401 (2022).
 - [14] T. Wang, N. F. Q. Yuan, and L. Fu, *Phys. Rev. X* **11**, 021024 (2021).
 - [15] J. Wang, J. Cano, A. J. Millis, Z. Liu, and B. Yang, *Phys. Rev. Lett.* **127**, 246403 (2021).
 - [16] E. Khalaf, S. Chatterjee, N. Bultinck, M. P. Zaletel, and A. Vishwanath, *Sci. Adv.* **7**, eabf5299 (2021).
 - [17] C. De Beule, F. Dominguez, and P. Recher, *Phys. Rev. B* **104**, 195410 (2021).
 - [18] P. J. Ledwith, E. Khalaf, and A. Vishwanath, *Ann. Phys.* **435**, 168646 (2021).
 - [19] O. Vafek and J. Kang, *Phys. Rev. B* **104**, 075143 (2021).
 - [20] V. T. Phong, P. A. Pantaleón, T. Cea, and F. Guinea, *Phys. Rev. B* **104**, L121116 (2021).
 - [21] J. S. Hofmann, E. Khalaf, A. Vishwanath, E. Berg, and J. Y. Lee, *Phys. Rev. X* **12**, 011061 (2022).
 - [22] Y. Cao, D. Rodan-Legrain, J. M. Park, N. F. Q. Yuan, K. Watanabe, T. Taniguchi, R. M. Fernandes, L. Fu, and P. Jarillo-Herrero, *Sci. Adv.* **372**, 264 (2021).
 - [23] C. Shen, P. J. Ledwith, K. Watanabe, T. Taniguchi, E. Khalaf, A. Vishwanath, and D. K. Efetov, *Nat. Mater.* **22**, 316 (2023).
 - [24] D. Guerci, Y. Mao, and C. Mora, [arXiv:2305.03702](https://arxiv.org/abs/2305.03702).
 - [25] T. Devakul, P. J. Ledwith, L.-Q. Xia, A. Uri, S. de la Barrera, P. Jarillo-Herrero, and L. Fu, *Sci. Adv.* **9**, eadi6063 (2023).
 - [26] G. Tarnopolsky, A. J. Kruchkov, and A. Vishwanath, *Phys. Rev. Lett.* **122**, 106405 (2019).
 - [27] J. Wang, Y. Zheng, A. J. Millis, and J. Cano, *Phys. Rev. Res.* **3**, 023155 (2021).
 - [28] L. A. Navarro-Labastida and G. G. Naumis, *Phys. Rev. B* **107**, 155428 (2023).
 - [29] R. Bistritzer and A. H. MacDonald, *Proc. Natl. Acad. Sci. USA* **108**, 12233 (2011).
 - [30] L. A. Navarro-Labastida, A. Espinosa-Champo, E. Aguilar-Mendez, and G. G. Naumis, *Phys. Rev. B* **105**, 115434 (2022).
 - [31] D. Guerci, Y. Mao, and C. Mora, [arXiv:2308.02638](https://arxiv.org/abs/2308.02638).
 - [32] P. J. Ledwith, G. Tarnopolsky, E. Khalaf, and A. Vishwanath, *Phys. Rev. Res.* **2**, 023237 (2020).
 - [33] F. K. Popov and A. Milekhin, *Phys. Rev. B* **103**, 155150 (2021).
 - [34] S. A. Herrera and G. G. Naumis, *Phys. Rev. B* **104**, 115424 (2021).
 - [35] F. K. Popov and G. Tarnopolsky, [arXiv:2305.16385](https://arxiv.org/abs/2305.16385).
 - [36] F. K. Popov and G. Tarnopolsky, [arXiv:2303.15505](https://arxiv.org/abs/2303.15505).
 - [37] J. Dong, P. J. Ledwith, E. Khalaf, J. Y. Lee, and A. Vishwanath, *Phys. Rev. Res.* **5**, 023166 (2023).
 - [38] P. J. Ledwith, A. Vishwanath, and D. E. Parker, [arXiv:2209.15023](https://arxiv.org/abs/2209.15023).
 - [39] T. Ozawa and B. Mera, *Phys. Rev. B* **104**, 045103 (2021).
 - [40] B. Mera and T. Ozawa, [arXiv:2304.00866](https://arxiv.org/abs/2304.00866).
 - [41] A. Ramires and J. L. Lado, *Phys. Rev. Lett.* **121**, 146801 (2018).
 - [42] T. Stauber, T. Low, and G. Gómez-Santos, *Phys. Rev. Lett.* **120**, 046801 (2018).
 - [43] C. Xu and L. Balents, *Phys. Rev. Lett.* **121**, 087001 (2018).
 - [44] B. Andrews and A. Soluyanov, *Phys. Rev. B* **101**, 235312 (2020).
 - [45] M. Rodríguez-Vega, M. Vogl, and G. A. Fiete, *Phys. Rev. Res.* **2**, 033494 (2020).
 - [46] Y. Fu, E. J. König, J. H. Wilson, Y.-Z. Chou, and J. H. Pixley, *npj Quantum Mater.* **5**, 71 (2020).
 - [47] J. González and T. Stauber, *Phys. Rev. B* **102**, 081118(R) (2020).
 - [48] S. Liu, E. Khalaf, J. Y. Lee, and A. Vishwanath, *Phys. Rev. Res.* **3**, 013033 (2021).
 - [49] P. J. Ledwith, A. Vishwanath, and E. Khalaf, *Phys. Rev. Lett.* **128**, 176404 (2022).
 - [50] N. Benlakhrouy, A. Jellal, H. Bahlouli, and M. Vogl, *Phys. Rev. B* **105**, 125423 (2022).
 - [51] P. A. Pantaleón, V. T. Phong, G. G. Naumis, and F. Guinea, *Phys. Rev. B* **106**, L161101 (2022).
 - [52] P. A. Pantaleón, H. Sainz-Cruz, and F. Guinea, [arXiv:2310.13743](https://arxiv.org/abs/2310.13743).
 - [53] A. Sinner, P. A. Pantaleón, and F. Guinea, *Phys. Rev. Lett.* **131**, 166402 (2023).
 - [54] Y. Xie, A. T. Pierce, J. M. Park, D. E. Parker, E. Khalaf, P. Ledwith, Y. Cao, S. H. Lee, S. Chen, P. R. Forrester *et al.*, *Nature (London)* **600**, 439 (2021).
 - [55] G. G. Naumis, L. A. Navarro-Labastida, E. Aguilar-Méndez, and A. Espinosa-Champo, *Phys. Rev. B* **103**, 245418 (2021).
 - [56] E. Khalaf, A. J. Kruchkov, G. Tarnopolsky, and A. Vishwanath, *Phys. Rev. B* **100**, 085109 (2019).
 - [57] D. Matsumoto, T. Mizoguchi, and Y. Hatsugai, *J. Phys. Soc. Jpn.* **92**, 034705 (2023).

- [58] T. Mizoguchi, Y. Kuno, and Y. Hatsugai, *Phys. Rev. A* **102**, 033527 (2020).
- [59] T. Mizoguchi and Y. Hatsugai, *Phys. Rev. B* **107**, 094201 (2023).
- [60] T. Yoshida, T. Mizoguchi, Y. Kuno, and Y. Hatsugai, *Phys. Rev. B* **103**, 235130 (2021).
- [61] T. Mizoguchi, Y. Kuno, and Y. Hatsugai, [arXiv:2308.03971](https://arxiv.org/abs/2308.03971).
- [62] J. Wang, S. Klevtsov, and Z. Liu, *Phys. Rev. Res.* **5**, 023167 (2023).
- [63] Y. Sheffer and A. Stern, *Phys. Rev. B* **104**, L121405 (2021).
- [64] B. Castaing, Y. Gagne, and E. Hopfinger, *Physica D* **46**, 177 (1990).
- [65] A. de Jesús Espinosa-Champo and G. G. Naumis, *J. Phys.: Condens. Matter* **36**, 015502 (2024).
- [66] G. G. Naumis, R. A. Barrio, and C. Wang, *Phys. Rev. B* **50**, 9834 (1994).
- [67] G. G. Naumis, C. Wang, and R. A. Barrio, *Phys. Rev. B* **65**, 134203 (2002).
- [68] P. Roman-Taboada and G. G. Naumis, *Phys. Rev. B* **95**, 115440 (2017).
- [69] P. Roman-Taboada and G. G. Naumis, *Phys. Rev. B* **96**, 155435 (2017).
- [70] F. Arscott, *Periodic Differential Equations: An Introduction to Mathieu, Lamé, and Allied Functions* (The Macmillan Company, New York, 1964).
- [71] I. Kovacic, R. Rand, and S. Mohamed Sah, *Appl. Mech. Rev.* **70**, 020802 (2018).
- [72] F. J. López-Rodríguez and G. G. Naumis, *Phys. Rev. B* **78**, 201406 (2008).
- [73] F. J. López-Rodríguez and G. Naumis, *Philos. Mag.* **90**, 2977 (2010).
- [74] V. G. Ibarra-Sierra, J. C. Sandoval-Santana, A. Kunold, S. A. Herrera, and G. G. Naumis, *J. Phys.: Mater.* **5**, 014002 (2022).
- [75] P. San-Jose, J. González, and F. Guinea, *Phys. Rev. Lett.* **108**, 216802 (2012).
- [76] L. A. N. Labastida and G. G. Naumis, *Rev. Mex. Fis.* **69**, 1 (2023).
- [77] M. Hitrik, Z. Tao, and M. Zworski, [arXiv:2310.19140](https://arxiv.org/abs/2310.19140).
- [78] E. Andrade, F. López-Urías, and G. G. Naumis, *Phys. Rev. B* **107**, 235143 (2023).
- [79] X. Liu, C.-L. Chiu, J. Y. Lee, G. Farahi, K. Watanabe, T. Taniguchi, A. Vishwanath, and A. Yazdani, *Nat. Commun.* **12**, 2732 (2021).